How to Pare a Pair: Topology Control and Pruning in Intertwined Complex Networks.

Felix Kramer[1,2,3] and Carl D. Modes[2,3,4]

[1] *International Max Planck Research School for Cell, Deveplopmental and Systems Biology, Dresden, Germany*

[2] *Max Planck Institute for Molecular Cell Biology and Genetics (MPI-CBG), Dresden, Germany*

[3] *Center for Systems Biology Dresden (CSBD), Dresden, Germany*

[4] *Physics of Life (PoL), Dresden, Germany*

(Dated: 25. Februar 2020)

Recent work on self-organized remodeling of vasculature in slime-mold, leaf venation systems and vessel systems in vertebrates has put forward a plethora of potential adaptation mechanisms. All these share the underlying hypothesis of a flow-driven machinery, meant to prune primary plexi in order to optimize the system's dissipation, flow uniformity, or more, with different versions of constraints. Nevertheless, the influence of environmental factors on the long-term adaptation dynamics as well as the networks structure and function have not been fully understood. Therefore, interwoven capillary systems such as found in the liver, kidney and pancreas, present a novel challenge and key opportunity regarding the field of coupled distribution networks. We here present an advanced version of the discrete Hu-Cai model, coupling two spatial networks in 3D. We show that spatial coupling of two flow-adapting networks can control the onset of topological complexity in concert with short-term flow fluctuations. Further, our approach results in an alternative form of Murray's law, which incorporates local vessel interactions and flow interactions. This scaling law allows for the estimation of the model parameters in ideal Kirchhoff networks and respective experimentally acquired network skeletons.

I. INTRODUCTION

Many recent studies on biological transportation networks have been focused on the hypothesis that vasculature is remodelled according to the flow-induced stress sensed by the cells making up the tissue [1]. This self-organized process optimizes the structures for the task at hand (distributing oxygen and nutrients, getting rid of waste, carrying local secretion). The actual tissue response is dependent on the time-scales probed, as short-term changes usually concern rapid vessel diameter changes in response to pressure fluctuations or medication, while long-term effects e.g. due to metabolic changes may manifest in permanent diameter changes [2], usually leaving the vessel structure with a trade-off between efficiency and redundancy [3].

Particular focus has been directed to the remodelling of the capillary plexus and other rudimentary transport systems in the early developmental stages of organisms, i.e. by studying complex signalling cascades involving growth factors like VEGF in vascular systems of mammals [4] or auxin in plants [5]. Yet, the onset of refinement seems to be correlated with mechanical stresses (such as shear flow) as has been shown in a variety of model organisms like chicken embryo[1, 6], zebrafish[7], leaves[8] and slime mold [9].

Early theoretical approaches by Murray [10, 11] posited that diameter adaptation would minimize the overall power dissipation of the system. Following this of ansatz of network optimization, many recent models using global optimization schemes on expanded vessel networks (where diameter adaptation may lead to link pruning) involving random damage, flow fluctuations or rescaled volume costs were able to account for the trade-off of shunting and redundancies [12–14]. Further advances were made in empirical studies of local vessel dynamics, e.g. blood vessel systems [15–17] as well as derived by constructing Lyapunov functions describing the networks' effective maintenance cost [18]. It has further been shown that the outcomes of locally adapting networks are robust against variations of the initial topological structure [19] and that plexus growth and correlated flow fluctuations can provide elaborate hierarchies [3, 20]. Many of these effects may also be seen in continuous adaptation models in porous media [21, 22]. It is interesting and important to note here that these adaptation mechanisms may leave certain fingerprints in the form of scaling laws, both allometric [23] and geometric [24].

These studies typically involve volume or metabolic constraints applied to abstract Kirchhoff networks. Yet they disregard the key characteristic common to all fluid transport systems: spatial embedding, which matters especially in the case of capillary systems as these directly interact via transport of metabolites with the surrounding tissue. These systems have to maintain a robust structure while being embedded in a possibly stiff tissue environment potentially perturbing the shear stress driven adaptation mechanism.

We here focus on the development and function of multicomponent flow networks, which influence each other based on their spatial architecture. Biologically speaking, these systems often consist primarily of blood vessels

and a secondary entangled, interacting system as found for example in liver lobule [25–28], the kidney's nephrons [29, 30], the pancreas [31–33] or the lymphatic system [34]. Our ansatz may also be interpreted as one flow network being 'caged' by another complementary structure, which would make it fit to describe vessel systems embedded in stiff tissues, e.g. bone marrow [35].

In this work we study the adaptation of two coupled spatial networks according to an advanced version of the discrete Hu-Cai model [18] including Corson fluctuations[14]. Each network is subject to flow driven and volume-constrained optimization on its own. Meanwhile we introduce the networks' interaction in the form of a mutual repulsion or attraction of vessel surfaces. Repulsion will prevent them from touching directly by their otherwise flow driven radius expansion, introducing a competition of the two networks for the abundant space they are embedded in. Alternatively vessel surfaces could be be attracted towards each other, presenting a positive feedback towards maintaining intertwined structures. In combination with fluctuation induced redundancy, we find mutual repulsion to greatly reduce the networks relative loop density even when strong fluctuations are present. On the other hand we observe the emergence of another sharp transition towards a loopy state due to attraction between the two networks.

Unfortunately few metrics provide the means to fit or estimate the applied parameters of adaptation models to real systems, even though time-lapse experiments [7], counting pruning events and topology analysis on pruned structures [3, 36, 37] allow for qualitative insights into the mechanism at hand for certain model organisms. Yet there was no proposal to our knowledge to quantitatively acquire or fit the model parameters from real, pruned network structures. In particular, interwoven systems present a challenge as typical experimental setups for a full 3D reconstruction involve invasive measures, i.e. sacrificing the specimen and preventing any long-term vessel observation. To tackle that problem we generalize an important scaling law, which has been discussed again recently in this context [38]: Murray's Law. This generalization enables us to reconstruct the model parameters with high fidelity for Kirchhoff networks solely from a given graph topology and it's edge radii distribution (assuming the pruning process reached a stationary state). In the same manner we find a reasonable estimation for the parameters in experimentally acquired data sets of an interwoven system: sinusoids and canaliculi in the mouse's liver acinus.

We begin our study in section II with a brief reminder of the hydrodynamical and network theoretical background on which we operate. Next we set up our model framework and its crucial components in detail. In section III we present the numerical evaluation of our model, in particular illuminating the cases of repulsive and attractive coupling between networks. In section IV we test the generalized scaling laws on ideal Kirchhoff networks and on datasets of vessel networks provided by our collaborators. We then go on to discuss the implications and limits of our model framework in the concluding section V.

II. THEORETICAL FRAMEWORK

A. Kirchhoff networks

We model flow distribution networks as a composition of m rigid cylindrical tubes (referred to as edges) of given length l and radius r carrying a laminar flow, which are linked together by n branching points (referred to as vertices). Every cyclic path, meaning a progression of incident edges, which starts and terminates at the same vertex, will be referred to as loop. We assume a constant pressure drop Δp over the tube defined by the difference of its entry- and terminal-point hydrostatic pressures p. The fluid considered has viscosity η and by including no-slip boundary conditions, one can derive the volume flow rate f as the Hagen-Poiseuille law $f = \left(\frac{\pi r^4}{8\eta l}\right)\Delta p$ [39]. We assign a flow f_e, a pressure-drop Δp_e and a conductivity $c_e = \frac{f_e}{\Delta p_e}$ to every edge. Likewise we assign a source or sink s_j as well as a nodal pressure p_j to every vertex. This means the overall flow landscape may be determined together with incidence matrix $\boldsymbol{B}$ in vectorial form:

$$\boldsymbol{B}\cdot\boldsymbol{f} = \boldsymbol{s} \tag{1}$$

$$\boldsymbol{f} = \boldsymbol{C}\cdot\Delta\boldsymbol{p} = \boldsymbol{C}\cdot\left(\boldsymbol{B}^T\cdot\boldsymbol{p}\right) \tag{2}$$

with $\boldsymbol{s}\in\mathbb{R}^n$, $\boldsymbol{f}\in\mathbb{R}^m$, $\boldsymbol{B}\in\mathbb{R}^{n\times m}$. Equation (1) is referred to as current law, which presents a mass conversation law for every vertex. Equation (2) presents the classic form of Ohm's law with nodal pressure $\boldsymbol{p}\in\mathbb{R}^n$, and conductivity matrix $\boldsymbol{C}\in\mathbb{R}^{m\times m}$, which is diagonal $C_{ef} = c_e\delta_{ef}$. Note that this calculation is not just restricted to laminar viscous flows but may be applied to any stationary transport process following the Thomson/Dirichlet principle as well as random walks of particles on a lattice [40, 41]. A general solution for the system (1), (2) may be constructed by means of the generalized inverse (denoted here as $[\cdot]^\dagger$ [42]). Further using the dissipation minimization argument one can deduce the unique solution for pressure differences to be [43, 44]:

$$\Delta\boldsymbol{p} = \boldsymbol{C}^{-1/2}\left[\boldsymbol{B}\cdot\boldsymbol{C}^{1/2}\right]^\dagger\boldsymbol{s} \tag{3}$$

Using the characteristics of the generalized inverse, equation (3) may also be rewritten in the form:

$$\boldsymbol{p} = \left[\boldsymbol{B}\cdot\boldsymbol{C}\cdot\boldsymbol{B}^T\right]^\dagger\boldsymbol{s} \tag{4}$$

This class of systems is often referred to as lumped systems or Kirchhoff networks, in analogy to simple electric circuits, for which a full mathematical treatment is abundant [45].

B. Defining effective costs and spatial coupling

In order to model biological transport networks such as those found in the liver lobule, see Figure 1a, we define a multilayer network consisting of two intertwined, yet spatially separate objects each consisting of edges e and e', with designated vessel radii r_e, $r_{e'}$. As underlying graph topology we choose from the graph skeletons of the triply-periodic minimal surfaces P ('dual' simple cubic), D ('dual' diamond cubic) or G ('dual' Laves) [46]. These systems present highly symmetric and complementary space filling graphs and enable us to construct well defined intertwined networks with clear local edge affiliations. We accordingly define such a local affiliation of edges: Every path $\boldsymbol{q} = \{e_i\}$ of edges forming a loop in its respective network is bound to enclose an edge e'_j of the other network. We refer to all edges from the tuple $\boldsymbol{q}$ as 'affiliated' with e'_n and vice versa.
We begin modeling each network as a simple cubic lattice, see Fig. 1b and 1c. Each edge in either network is affiliated with up to four other edges in the other network (this will naturally change for different graph topologies). As all theses edges are simply tubes in our model, we define the distance between affiliated tube surfaces to be,

$$\Delta r_{ee'} = L - (r_e + r_{e'}) \tag{5}$$

where L is the initial distance of the abstract network skeletons (equal to distance in case of simultaneously vanishing radii). In order to model a system of blood vessels which is entangled with a secondary secreting vessel network, we postulate that the respective tube surfaces must not fuse or touch directly, i.e. having $\Delta r_{ee'} = 0$. We do not incorporate periodic boundaries. For the networks' optimization we follow the conventional ansatz of minimization of flow dissipation and network volume, while including flow fluctuations as in [18]. Subsequently we begin by constructing a Lyapunov function $\Gamma \geq 0$ for the combined system [47]:

$$\Gamma = \sum_{e} \left[\frac{f_e^2}{c_e} + a v_e \right] + \sum_{e'} \left[\frac{f_{e'}^2}{c_{e'}} + a' v_{e'} \right] + E \tag{6}$$

introducing an 'energy density' E for the respective tube surfaces of the network edges

$$E = \frac{b}{2} \sum_{ee'} F_{ee'} \Delta r_{ee'}^{\varepsilon} \tag{7}$$

$$\text{with } F_{ee'} = \begin{cases} 1 & \text{if edges } e \text{ and } e' \text{affiliated} \\ 0 & \text{else} \end{cases} \tag{8}$$

with positive coefficients $a, a', b > 0$. As in [18] we consider a constant length scale l for all tubes, so we may rewrite the conductivity $k_e = l c_e = \frac{\pi}{8\eta} r_e^4$, which implies the changes of conductivity to be solely the result of radii adaptation. Additionally we set the volume penalty as $v_e = l r_e^2$. We define a pressure gradient as $\Delta\varphi_e = k_e^{-1} f_e$

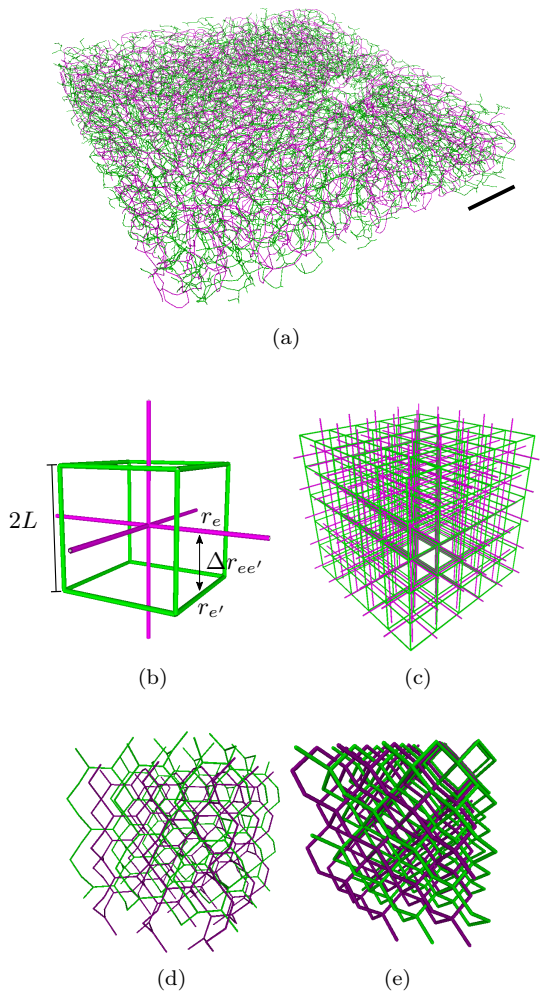

FIG. 1: (a) Biological intertwined structures: segment of bile canaliculi (green) and sinusoids (magenta) in the mouse's liver acinus (presented as network skeletons, see also [28])), scale bar is $200\mu m$. (b) - (e) Modelling two interacting networks and 3D network skeletons of triply-periodic minimal surfaces for initial plexi: (b) (Cubic) unit cell and indication of spatial constraint for tube surfaces. (c) Complementary cubic lattices (P surface) . (d) Complementary Laves lattices (G surface). (e) Complementary diamond lattices (D surface).

where $k_e = \frac{\pi r_e^4}{8\eta}$ are elements of the diagonal $\boldsymbol{K}$. We do not consider cost variations via an exponent $k_e \to k_e^{\gamma}$ as suggested in other studies [12, 18]. We minimize Γ using a gradient descent method choosing the radii dynamics to be $\partial_t r_e = -\chi \nabla_{r_e} \Gamma$, and vice versa for $\boldsymbol{r}_{e'}$ with auxiliary coefficients χ, $\chi' > 0$. If a given radius falls below a set threshold we prune it, i.e. we remove the respective edge from the graph. Details of the derivation of $\partial_t r_e$ are given in the supplementary material A .
In order to perform a numerical evaluation of the resulting ODE system we define a unit system as follows:

the radii in units of the grids' distance $r_e = Lr_e^*$, fluctuating nodal in and outflow $s_i = \mu s_i^*$, time $t = \frac{L^3}{\mu} t^*$, the conductivity $k_e = \eta^{-1} L^4 k_e^*$ and hence pressure $\Delta\varphi_e = \frac{\mu\eta}{L^4}\Delta\varphi_e^*$ and the networks' edge surface distance $\Delta r_{ee'}^{\varepsilon-1} = L^{\varepsilon-1}\Delta r_{ee'}^{*\varepsilon-1}$. We thus acquire the dimensionless form of the dynamical equations for each network:

$$\partial_{t^*} r_e^* = \lambda_0 \left(\Delta\varphi_e^{*2} r_e^{*3} - \lambda_2 r_e^* + \lambda_1 g_e^*\right) \tag{9}$$

with the effective temporal response parameters $\lambda_0 = \chi \left(\frac{\mu\eta}{L^3}\right)^2$, the effective network coupling $\lambda_1 = \frac{b|\varepsilon|L^{\varepsilon-2}}{\pi l \eta}\left(\frac{L^3}{\mu}\right)^2$ and the effective volume penalty $\lambda_2 = \frac{4a}{\pi\eta}\left(\frac{L^3}{\mu}\right)^2$. To construct the networks in a symmetric manner we set the respective tube-lengths equally $l = l'$. We set the effective coupling term as

$$g_e^* = sgn\left(\varepsilon\right) \sum_{e'} F_{ee'} \Delta r_{ee'}^{*\varepsilon-1} \tag{10}$$

using the sign function $sgn\left(\varepsilon\right)$. The coupling g_e^* changes its qualitative behavior with variation of the exponent ε. We will consider the cases of an attractive coupling $\varepsilon > 1$ and a repulsive coupling $\varepsilon < 0$, see Figure 2. We will further discuss the trivial case of an uncoupled system $\varepsilon = 0$ (for which $\lambda_1 = 0$) for direct comparison with the Hu-Cai model. Note that $\varepsilon = 1$ will result in a constant g_e^* corresponding to a positive constant background stimuli, as proposed by [20]. The case $0 < \varepsilon < 1$ results in a diverging attraction for nearby vessels, while it basically drops out for $\Delta r_{ee'} \longrightarrow 1$. These numeric and heuristically unfavorable cases of $0 < \varepsilon < 1$ as well as the linear case $\varepsilon = 1$ will be neglected hereafter.

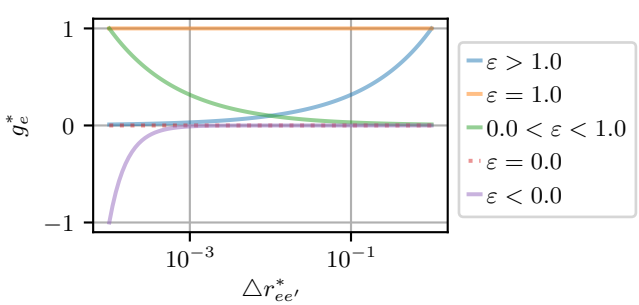

FIG. 2: The effective behavior of the coupling term g_e^* changes with variation of the exponent ε . Function values of g_e^* are presented here dependent on the distance of a single arbitrary vessel pairing, curves normalized for comparison.

C. Incorporating flow fluctuations: Noisy, uncorrelated sink patterns

W next assume the adaptation of the vascular networks depends on an averaged potential landscape instead of instantaneous configurations, which are bound to occur in real systems due to short-term metabolic changes or vessel blocking/damage. I.e. we assume a constant vessel radius between two adaptation events, while the flow rates change throughout the system due to changes in the sinks' magnitude, enabling us to substitute $\Delta\varphi_e^2 \to \langle\Delta\varphi_e^2\rangle$ in equation (9). This incorporates the assumption of a time-scale separation between the radii adaptation (long-time changes, not to be confused with short term contraction/dilation) and changes of hydrostatic pressure. We define fluctuations in accordance to the Corson model [14]. Subsequently we only consider $\boldsymbol{s}$-configurations in which there exists one source-node (here $j = 0$, $s_0 = -\sum_{j>0} s_j$) and all other nodes are randomly initialized sinks with the following characteristics:

$$\langle s_j \rangle = \mu_j \text{ with } j > 0 \tag{11}$$

$$\langle s_j s_k \rangle = \rho_{jk}\sigma_j\sigma_k + \mu_j\mu_k \text{ with } j,k > 0 \tag{12}$$

This enables us to calculate the mean squared pressure as,

$$\langle\Delta\varphi_e^2\rangle = \left\langle \left(\boldsymbol{K}^{-1/2}\left[\boldsymbol{B}\cdot\boldsymbol{K}^{1/2}\right]^{\dagger}\boldsymbol{s}\right)_e^2 \right\rangle = \sum_{j,k=0}^{n,n} \boldsymbol{A}_{jk}^e \langle s_j s_k\rangle \tag{13}$$

with an auxiliary conductivity tensor $\boldsymbol{A}_{jk}^e = k_e^{-1}\left[\boldsymbol{B}\cdot\boldsymbol{K}^{1/2}\right]_{ej}^{\dagger}\left[\boldsymbol{B}\cdot\boldsymbol{K}^{1/2}\right]_{ek}^{\dagger}$. We assume the fluctuations are uncorrelated and follow the same probability distribution. We set for the mean $\mu_j = \mu$, standard deviation $\sigma_j = \sigma$, and correlation coefficient $\rho_{jk} = \delta_{jk}$. We may subsequently calculate the average squared pressure:

$$\langle\Delta\varphi_e^2\rangle = \mu^2\phi_e + \sigma^2\delta\phi_e \tag{14}$$

with the edge-potential functions ϕ_e, $\delta\phi_e$ defined as

$$\phi_e = \sum_{jk} \boldsymbol{A}_{jk}^e \boldsymbol{U}_{jk} \tag{15}$$

$$\delta\phi_e = \sum_{jk} \boldsymbol{A}_{jk}^e \boldsymbol{V}_{jk} \tag{16}$$

and coefficient matrices

$$\boldsymbol{V}_{jk} = \delta_{jk} + \left(n + 1 + \delta_{jk}\right)\delta_{0j}\delta_{0k} - \left(1 + \delta_{jk}\right)\left(\delta_{0j} + \delta_{0k}\right) \tag{17}$$

$$\boldsymbol{U}_{jk} = 1 + \delta_{0j}\delta_{0k}n^2 - n\left(\delta_{0j} + \delta_{0k}\right) \tag{18}$$

It may be noted here that $\boldsymbol{A}^e\boldsymbol{U}$ describes the constant squared pressure in case of a constant source-sink landscape in the absence of any variance σ^2. Hence $\boldsymbol{A}^e\boldsymbol{V}$ describes the pressure perturbation caused by fluctuations of strength σ^2 in correspondence to the Hu-Cai models heuristic fluctuation ansatz. The detailed form of $\boldsymbol{U}$, $\boldsymbol{V}$ depends on the positioning of sinks and sources in the

system. For the full derivation of equations (15), (16) and the respective coefficient matrices (17), (18) see Appendix B. Using this approach we prevent shunting and the generation of spanning trees, which is caused by the typical 'single source - multiple sinks' setting. Further, using this ansatz one also prevents accidentally partitioning the graph as opposed to realizing the sink-source configurations one by one [3].
We find this ansatz in particular fitting to model the liver lobule system, as sinusoids are fenestrated structures (meaning the vessel wall is perforated). Additionally bile and water is frequently secreted by hepatocytes (cells forming the bulk of tissue and basic metabolic unit in the liver) into bile canaliculi. On the other hand one may argue that the fluid leak in the sinusoidal system is negligible in comparison to the overall throughput rate, and an additional distinguished sink would have to be placed at the opposing end of the plexus, extracting the majority of fluid. Here we neglect this factor as one major sink would merely generate one (or a small number of) distinguished large vessel(s), without any further impact on the topological complexity of the rest of the networks. We incorporate these flow fluctuations with the rescaled mean squared pressure and an effective flow-fluctuation $\lambda_3 = \frac{\sigma^2}{\mu^2}$ in equation (9):

$$\partial_{t^*} r_e^* = \lambda_0 \left(\left(\phi_e^* + \lambda_3 \delta \phi_e^* \right) r_e^{*3} - \lambda_2 r_e^* + \lambda_1 g_e^* \right) \qquad (19)$$

The parameters λ_0', λ_1', λ_2' and λ_3', describing the second network with indices e', are constructed analogously.

III. NUMERICAL EVALUATION OF THE MODEL FRAMEWORK

The optimization according to equation (19) is performed until the edge radii reach a stationary state. We solve these equations numerically with the Heun scheme using a manually adjusted increment of $h \leq 10^{-4}$. We set the fluctuation rates identical $\lambda_3 = \lambda_3'$ and proceed likewise with coupling strength $\lambda_1 = \lambda_1'$. During this optimization we mark edges whose radius falls below a critical threshold ρ_c. These edges are no longer updated and are considered to have a radius of virtually zero (though for computational reasons they are here set to $\rho_c = 10^{-21}$, these edges are referred to as pruned). The graphs consisting of m_c and m_c' non-pruned edges are then analyzed for their cyclic structure. We calculate the number of the independent loops (nullity) in the final network as proposed in[48]. We use the relative nullity of a graph as $\varrho = \frac{m_c - n + 1}{l_0}$ as an order parameter, where l_0 is the initial number of independent loops. All diagrams shown represent the results for one network; the results are highly symmetric for the other network due to the symmetric choices of parameters λ_i, λ_i', see Appendix C for further details.

A. Uncoupled adapting networks: $\varepsilon = 0$

First, we test the original Hu-Cai model in combination with Corson's fluctuation approach in our 3D setting, i.e. the uncoupled case of $\varepsilon = 0$. The initial edge radii are chosen randomly. We calculate the adaptation of simple cubic networks with a single corner source node (sinks otherwise) for a systematic scan of λ_2, λ_3, see Figure 3. We can show the transition from tree like configurations for $\lambda_3 \leq 1$, see 3a, towards states exhibiting fluctuation induced loops for large λ_3, see 3b. The emerging transition is of logarithmic nature, saturating for $\lambda_3 \approx 10^4$. In particular we can confirm that in agreement with Hu-Cai [18] that only an increase in the fluctuation ratio λ_3 results in an increase of nullity, see 3c. The continuous transition observed is independent of the system's effective volume penalty λ_2, see 3d. Note that the parameters λ_2, λ_2' influence the final vessel diameter as well as the time scales for reaching the stationary state (as does the system size if the number of identical sinks scales with system size).

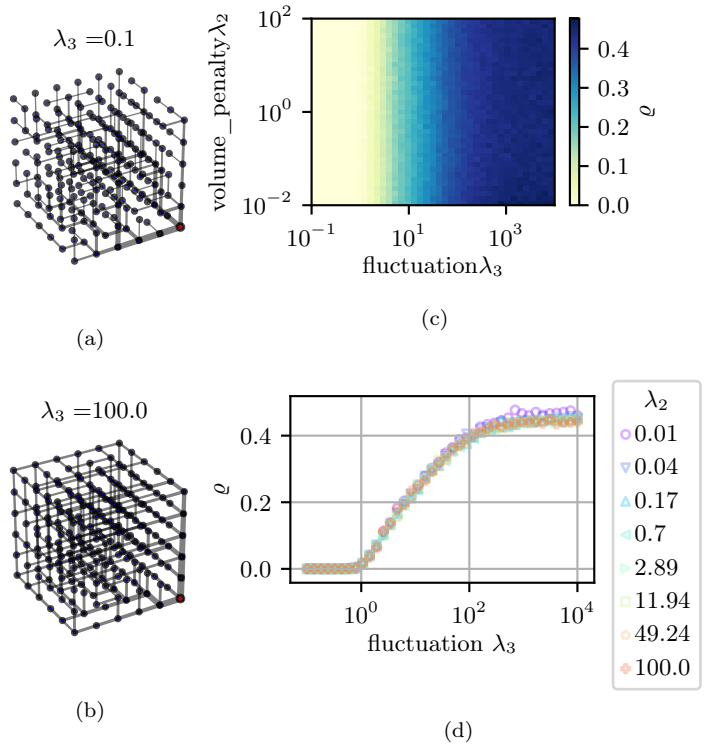

FIG. 3: Stationary network configurations for $\lambda_2 = 1$. The edge thickness is representative for the relative tube radius ρ. Sinks are marked as blue dots, the source as large red circle. (a) Tree-like for $\lambda_3 = 0.1$ (b) Fluctuation induced loops for $\lambda_3 = 100$. (c) + (d) Uncoupled adapting networks display continuous, logarithmic λ_2-independent nullity ϱ transitions ($\lambda_1 = 0$, cubic lattice, $n = 216$ and $m = 540$).

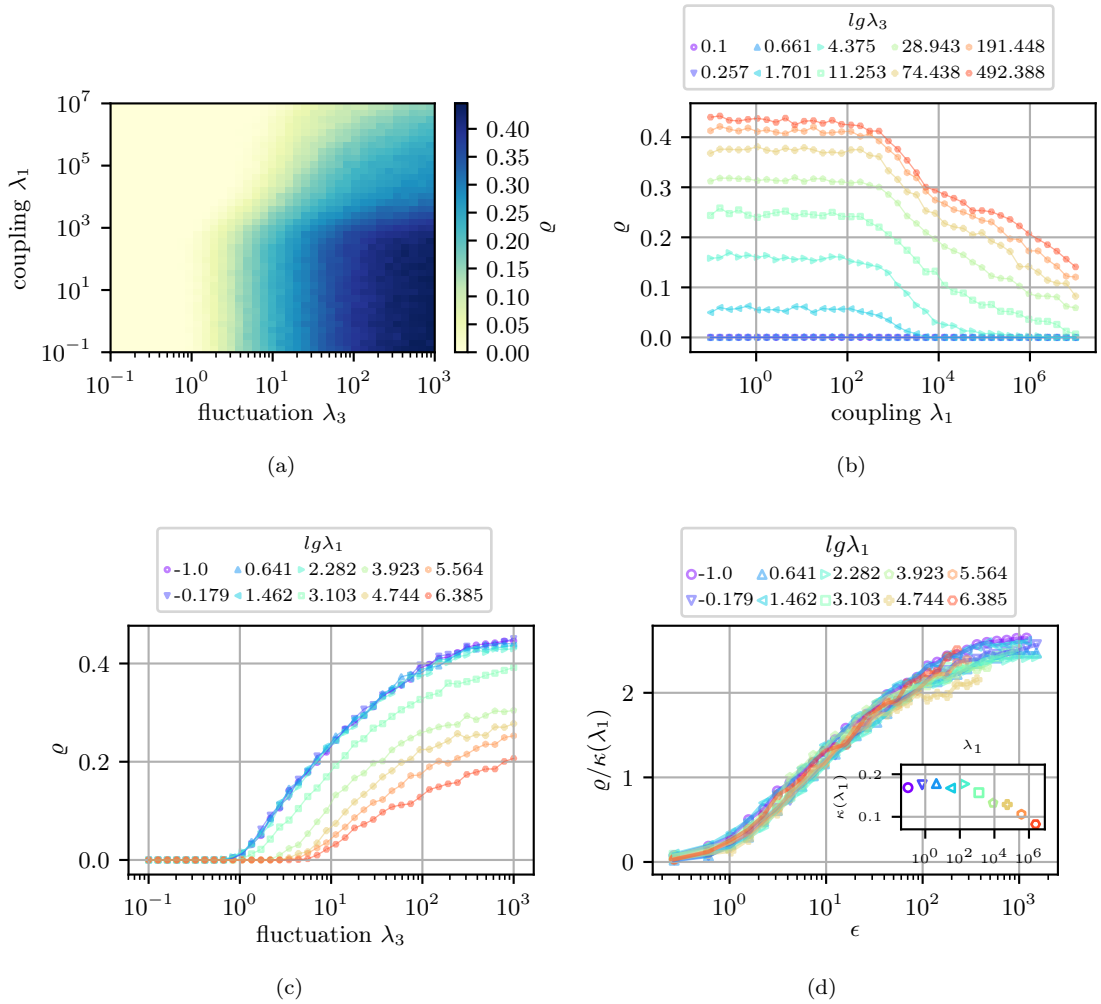

FIG. 4: Nullity ϱ transitions and state diagram for a repulsively coupled network ($\varepsilon = -1$): (a) Coupling vs fluctuation, (λ_1, λ_3)-diagram as nullity ϱ colormap. (b) Coupling λ_1 induced nullity breakdown for varying fluctuation λ_3. (c) Fluctuation λ_3 induced nullity onset for varying coupling λ_1. (d) Single curve collapse near fluctuation induced nullity onset λ_c, rescaled as $\epsilon = \frac{\lambda_3 - \lambda_c}{\lambda_c}$ and scaled nullity $\varrho/\kappa(\lambda_3)$. We find the transition to be approximated by $\varrho(\lambda_1, \lambda_3) \approx \kappa(\lambda_1)(lg\epsilon - 1)$, the scale κ is shown in the inset.

B. Coupled adapting networks: Repulsive coupling $\varepsilon < 0$

We now turn to the novel, spatially coupled cases, systematically scanning the effective network coupling and flow-fluctuation parameters. For these simulations we set the response $\lambda_0 = \lambda_0' = 10^{-4}$, and volume penalty $\lambda_2 = \lambda_2' = 10^6$ (providing reasonable computation times for reaching stationary states and preventing the problem becoming too stiff). The repulsion's exponent is set $\varepsilon = -1$. The initial edge radii are chosen randomly (with all affiliated edge pairs fulfilling $0 < r_e^* + r_{e'}^* < 1$). The state diagram 4a shows that the system's nullity may be influenced not only by the rate of fluctuation λ_3, but by the repulsion of the two networks as well. In Figure 4b we show the corresponding λ_1 induced breakdown, displaying the possibility to nullify any reticulated structures by increasing the repulsive coupling strength in the system. On the other hand, we find the nullity onset to be continuous in the system, starting from a tree-like state at small fluctuations and increasing monotonically in a logarithmic manner beyond a critical $\lambda_3 \geq \lambda_c$, see Figure 4c). Eventually, the ϱ-trajectory saturates for large fluctuation rates $\lambda_3 \to 10^3$ towards a maximal nullity ϱ_{max}. This leaves the network in a reticulated state, still displaying a visible vessel hierarchy towards the source. We can recover tree-like network states for increased repulsion rates λ_1 even losing the typical vessel hierarchy towards the source, see Figure 5. This increase in λ_1 is further shifting the nullity onset. To quantify these shifts we acquire the critical λ_c by identifying the logarithmic

transition's root in Figure 4c. It appears that the critical point λ_c becomes a monotonically increasing function of the coupling parameter λ_1. In Figure 4d we show the rescaled trajectories of 4c near the onset of the nullity transition. Introducing the reduced fluctuation parameter $\epsilon = \frac{\lambda_3 - \lambda_c}{\lambda_c}$ we find the transition to follow a trivial logarithmic law $\varrho(\lambda_1, \lambda_3) \approx \kappa(\lambda_1)(lg\epsilon - 1)$, with the coupling dependent scale κ shown in the inset of Figure 4d. Generating these state-diagrams for the respective network skeletons of D (diamond lattices) and G surfaces (Lave graphs), we found no qualitative differences arising from altered plexus topology.

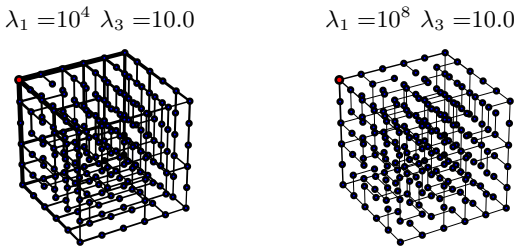

FIG. 5: Stationary network configurations for $\lambda_2 = 10^6$. The edge thickness is representative for the relative tube radius r^*. Sinks are marked as blue dots, the source as a large red circle. Repulsive coupling causes nullity breakdown and overall reduction in edge thickness leading to the disappearance of the usual vessel hierarchy.

C. Coupled adapting networks: Attractive Coupling for $\varepsilon > 1$

We now consider intertwined networks with an attractive spatial coupling. For these simulations we set the response $\lambda_0 = \lambda_0' = 10^{-4}$, and volume penalty $\lambda_2 = \lambda_2' = 10^6$ as before. The parameter λ_3 is only considered here for $\lambda_3 < 300$ as affiliated edge pairs will violate the contact condition $0 < r_e^* + r_{e'}^* < 1$ beyond this range.We initialize the system here for a positive coupling exponent $\varepsilon = 3$. This leads to a major change in the system nullity behavior, see Figure 6, as an additional positive feedback term is introduced in equation (19). In Figure 7 we show the resulting nullity state diagrams and transition curves. For increasing coupling strength λ_1 a new nullity transition emerges for $\lambda_1 > \lambda_c$, virtually recovering the initial plexus for $\lambda_1 \to 10^4$, see Figure 7b. Even though an increase in fluctuation λ_3 will generate an offset, the transition's form is well preserved. This may be clearly seen in Figure 7d as the transition zone may be collapsed onto one single trajectory as $\varrho(\lambda_3, \epsilon) \approx \kappa(\lambda_3)\epsilon + \varrho_0(\lambda_3)$, with rescaled x-axis $\epsilon = \frac{\lambda_1 - \lambda_c}{\lambda_c}$. The λ_3 dependency of the respective scaling parameters are shown in the insets of Figure 7d. We note here that these curves are slightly different from the complementary network in the case of cubic lattice topology as they are considerably more spread out. This phenomenon does not seem to be present in the case of Lave-graphs or diamond lattices. The fluctuation induced nullity transition on the other hand is perturbed and vanishes beyond the λ_1 transition, see Figure 7c . Yet, an underlying competition of mechanisms is observable for large λ_3 as the nullity again decreases towards a fluctuation dominated network structure. This interplay between different positive feedback mechanisms creates multiple nullity states, see Figure 7a, tuning the structures between spanning trees and fully recovered plexus. Generating these state-diagrams for the respective network skeletons of D and G surfaces, we found no qualitative differences arising from altered plexus topology, again observing the same complex behavior.

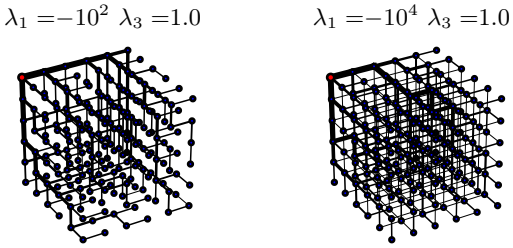

FIG. 6: Stationary network configurations for $\lambda_2 = 10^6$. The edge thickness is representative for the relative tube radius r^*. Sinks are marked as blue dots, the source as a large red circle. Attractive coupling sets another local positive feedback which fixes overall nullity to the point of total plexus recovery.

IV. GENERALIZING MURRAY'S LAW

Our model of spatial coupling also points to a new form of scaling at vessel branchings. We refer hereby to the concept of Murray's Law, connecting the radii r_0 of the parent vessel splitting into at least two child branches with radii r_1, r_2 as:

$$r_0^\alpha = r_1^\alpha + r_2^\alpha \tag{20}$$

Originally a cubic scaling exponent of $\alpha = 3$ was predicted as the outcome of a cost optimization process [10]. Further, rescaled costs models [12] which consider cost variations via an exponent $k_e \to k_e^\gamma$ suggest

$$\alpha = 2(\gamma + 1) \tag{21}$$

while discarding flow fluctuations. Testing these scaling laws for the network-skeletons of the sinusoids and bile canaliculi in the liver-lobule by fitting the exponent α

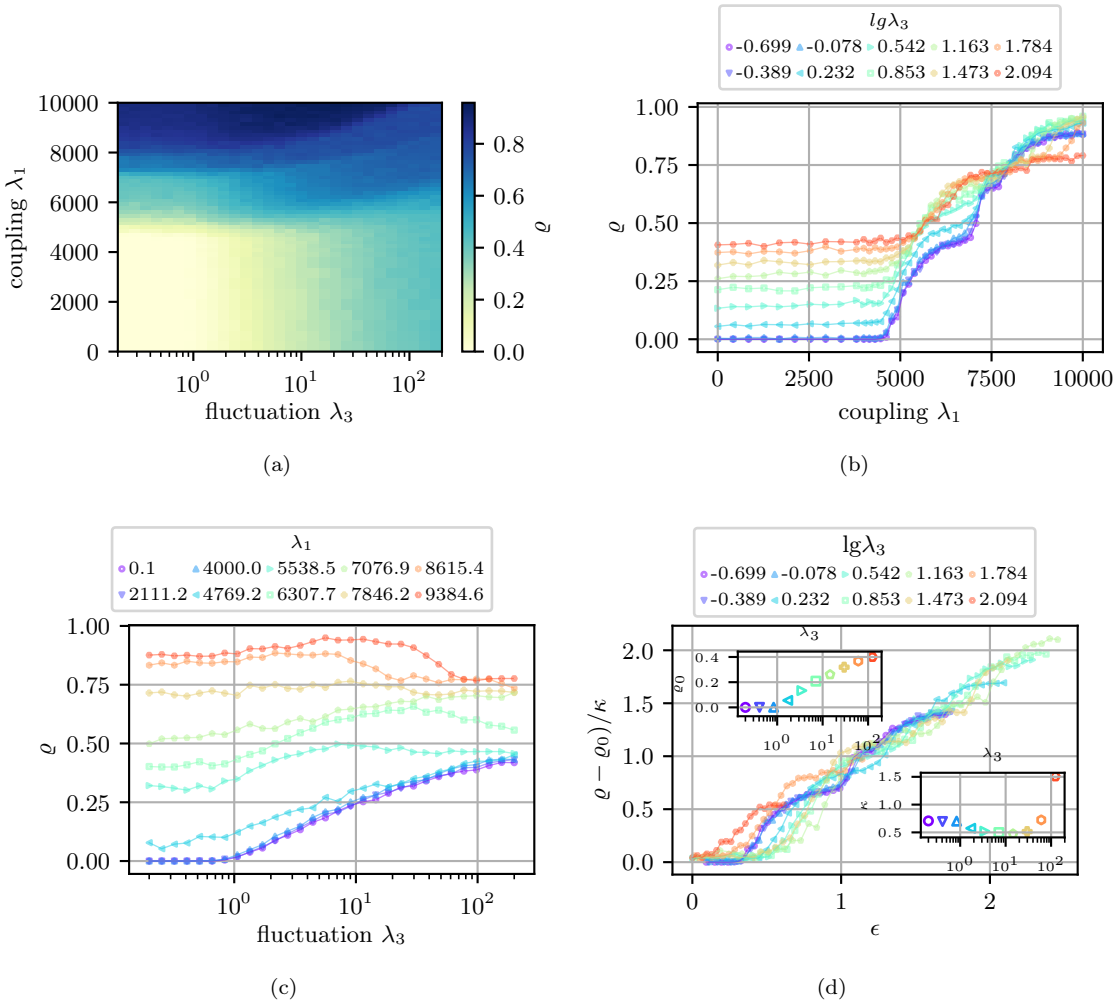

FIG. 7: Nullity ϱ transitions and state diagram for an attractively coupled network ($\varepsilon = 3$): (a) Coupling vs fluctuation, (λ_1, λ_3)-diagram as nullity ϱ colormap. (b) Coupling λ_1 induced nullity transition for varying fluctuation λ_3. (c) Fluctuation λ_3 induced nullity transition for varying coupling λ_1. (d) Single curve collapse near coupling induced nullity onset λ_c, rescaling as $\epsilon = \frac{\lambda_1 - \lambda_c}{\lambda_c}$ and scaled nullity $(\varrho - \varrho_0(\lambda_3))/\kappa(\lambda_3)$. We find the transition to be approximated by $\varrho(\lambda_1, \lambda_3) \approx \kappa(\lambda_3)\,\epsilon + \varrho_0$, the scale κ is shown in the inset.

in equation (20) for every branching of degree three (Y-branching), one can see that there is significant deviation from the predicted exponent $\alpha = 3$, see Figure 8. The acquired values are $\alpha \approx 3.75$ for sinusoids and for bile canaliculi $\alpha \approx 3.33$. As capillary systems were already known to defy the cubic relationship [24], we suspect this to be correlated with the reticulated nature of these networks. Further, this deviation is not well described by the cost exponent γ. In accordance to equation (21) one would deduce $\gamma < 1$ in liver lobule which is in direct contradiction with the rescaled cost model [12], which predicts the induced loops only for $\gamma \geq 1$. On the other hand this could be circumvented if fluctuation induced loops are considered as well [13, 14]. However to our knowledge it has not yet been discussed how these fluctuations alter Murray' Law. We may deduce from our pruning model a new set of coefficients a_e which are dependent on their corresponding edge's neighborhood and the respective coupling strength, as well as the global structure of sinks and sources (which were assumed to be uncorrelated and identically distributed). This procedure greatly alters the form of equation (20) and we derive a new scaling law derived from the steady-states of the ODEs in equation (19). We recover the cubic exponent of the original model with new coefficient corrections that depend on the strength of fluctuations and spatial

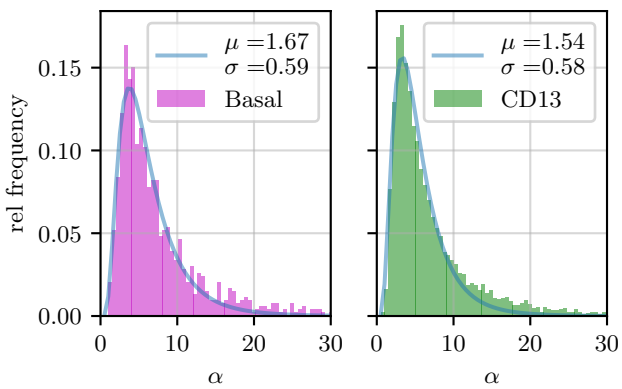

FIG. 8: Exponent distributions found for Murray's Law (20) and respective log-normal fits: Sinusoidal systems (basal marker) with mode $\alpha = e^{\mu-\sigma^2} \approx 3.75$ and bile canaliculi systems (cd13 marker) with mode $\alpha = e^{\mu-\sigma^2} \approx 3.33$.

coupling:

$$\sum_e a_e r_e^{*,3} = 1 \tag{22}$$

$$\text{with } a_e = \pm\sqrt{\frac{\lambda_2 + \lambda_1 r_e^{*,-1} g_e^*}{1 + \lambda_3 \frac{\delta\phi_e^*}{\phi_e^*}}}$$

The effective coupling $g_e^* = sgn\,(\varepsilon) \sum_{e'} F_{ee'} \Delta r_{ee'}^{*\varepsilon-1}$, and squared edge potentials ϕ_e^*, $\delta\phi_e^*$ are defined as in section II. The scaling law (22) may also be generalized in case of more complicated flow landscapes, see Appendix (22).

A. Estimating parameters from ideal Kirchhoff networks

We tested the feasibility of ansatz equation (22) by simulating the pruning on a dual Laves graph topology (3-regular), with $n = 206$ ($n' = 210$) vertices and $m = 259$ ($m' = 261$) edges and setting the parameters symmetrically to $\lambda_1 = \lambda_1' = 10^4$, $\lambda_2 = \lambda_2' = 10^6$, $\lambda_3 = \lambda_3' = 10^2$. The sources were positioned in random vertices of the system. Edges of the respective networks were affiliated with each other by finding the nearest neighbors of edges inside a perimeter δ. We numerically [49] find the roots of equation (22) for a set of positive definite λ_1, λ_2, λ_3 and λ_1', λ_2', λ_3' respectively. As we do not intend to use information on the direction of the currents at the sink-nodes (and this information is not available in the real system) we will solve equation (22) for the seven relevant sign permutations at each branching, see supplement Figure 1b. For further evaluation only the fit of highest quality (function value) is used. We use a logarithmic rescaling $x_i = log_{10}\lambda_i$ in order to find a symmetric representation of the histogram's data. Doing so we fit a normal distribution $\aleph(\mu, \sigma)$ to the distributions maxima and we find strong agreement with the actual parameters for both networks, see Figure 9c. We also tested for the abundance of multiple existing sources distributed throughout the system (acting as identical copies of each other). We find our procedure correctly identifying the relevant model parameters in this case as well, see Figure 9d.

B. Estimating parameters for sinusoidal networks

In this section we use the extracted graph skeletons of the sinusoids and bile canaliculi in the vicinity of a central vein in the mouse liver to test our model on a real intertwined vessel system. The vascular structure is thereby given to us by sets of vertices bearing the positional and radial information of the respective vasculature. We use the same approach as in the prior section to estimate the parameters λ_1, λ_2, λ_3 for the sinusoidal system, based on the available information of topology and radii distribution provided.

The datasets were acquired from collaborators at the MPI-CBG in the following way: Mouse livers from adult mice were fixed by trans-cardial perfusion, sectioned into 100 mm serial slices, optically cleared and immunostained, as described in [28]. To visualize the different tissue components, the tissue sections were stained for nuclei (DAPI), cell borders (Phalloidin), bile canaliculi network (CD13), and the extracellular matrix (ECM, fibronectin and laminin) facing the sinusoidal network[50]. High-resolution images of the liver lobule (Central vein – portal vein axis) were acquired by using confocal microscopy with a 63x/1.3 objective (0.3μm voxel size). Finally, the resulting images were segmented and network skeletons calculated with the Motion Tracking software as described in [28] and [51].

We stress that no information about the actual flow nor the exact point of flow injection or drainage was available. Hence we first make some simplifying assumptions about the position of sinks and sources as well as cropping the network-skeletons reducing their complexity: First we identify the vertices in the sinusoidal network which are closest to the central vein and label them as sinks. The geometric center of mass is calculated and used as the center of a sphere of radius R, representing the range of interest. Any other components, vertices or edges of any network positioned outside this perimeter are discarded (here $R = 390\mu m$, in order to keep the resulting graphs at a moderate size for computational purposes). Next, all branching points in the sinusoidal network are identified and all paths $\boldsymbol{p} = (e_i, ..., e_j)$ consisting of edges e_i which start from these points. We proceed for the canaliculi the same way and check for each segment of a path whether there is another segment of another network's path inside a perimeter δ (here chosen as $20\mu m$). If so, these paths count as affiliated. We merge all edges

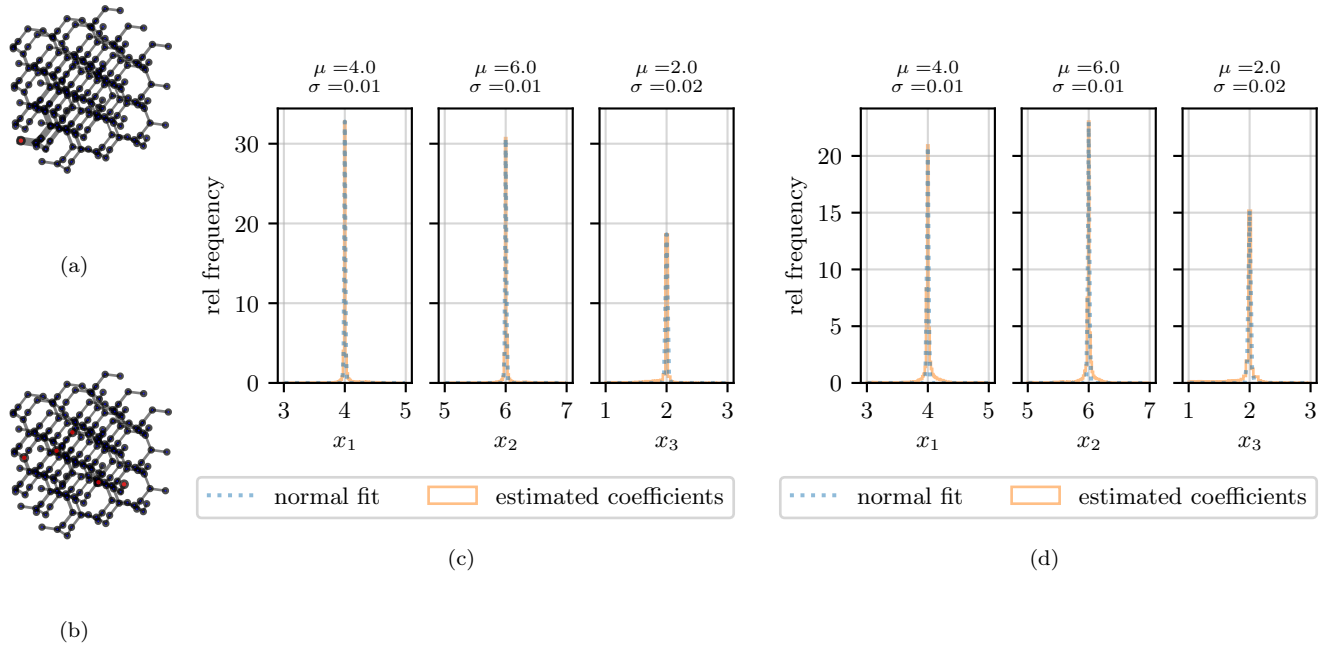

FIG. 9: Test of coupled ideal Kirchhoff networks, dual Laves-Graph topology, rescaled axis is $x_i = log_{10}\lambda_i$, the system was initialised symmetrically with $x_1 = 4$, $x_2 = 6$ and $x_3 = 2$ (a) + (c) : Single source-multi-sink system, parameters histograms and fits $\aleph(\mu, \sigma)$ presenting the estimated simulation parameters λ_i. Network plot of the respective reticulated network showing the source in red and sinks in blue. (b) + (d) : Multi-source-multi-sink system, parameters histograms and fits $\aleph(\mu, \sigma)$ presenting the estimated simulation parameters λ_i. Network plot of the respective reticulated network, showing the five initialized 'cloned' sources in red and sinks in blue.

along a path towards a single edge by using the conventional addition theorems for series of conductivities in Kirchhoff networks. Proceeding like this we end up with a reduced sinusoidal network, with $n = 318$ vertices and $m = 452$ edges. For further details on the reduction procedure see Figure 15 in Appendix D. From this we calculate the coupling and fluctuation terms in equation (22) for the cases of repulsive coupling $\varepsilon = -1$ and attractive coupling $\varepsilon = 3$, under consideration of all sign permutations for a_j. The solutions' histograms are presented in Figure 10, where we find the parameters for repulsive coupling to be roughly distributed at $x_1 = 3.08 \pm 1.55$, $x_2 = 3.02 \pm 0.68$, $x_3 = 1.04 \pm 0.83$. For attractive coupling we can estimate these distributed at $x_1 = 3.27 \pm 0.76$, $x_2 = 3.03 \pm 0.59$, $x_3 = 0.93 \pm 0.59$. Bear in mind the large standard deviation and asymmetric character of the error (due to the logarithmic scaling) which provides a significant level of uncertainty. Further, we found the choice of perimeters R, δ to affect the estimated parameter distributions presented in Figure 10, for further information see Figures 16 and 17 iin Appendix D. Nevertheless with this technique we have shown that it is possible to extract order of magnitude *estimates* of otherwise inaccessible parameters of real adapting biological networks.

V. DISCUSSION

We have shown that spatial coupling presents another potential mechanism of controlling the topological complexity of optimal transport systems in 3D. We considered the special case of 'single source to multiple sinks' in combination with simple cubic lattices as plexi as the simplest case possible. In the case of repelling networks we find this interaction to reduce the networks' relative loop density and provide another method by which a system may be tuned towards its final architecture. It's also possible to retrieve tree-like states at increased fluctuation levels, which imposes a new stabilization mechanism for spanning trees in noisy networks. Nevertheless the onset of redundancy is primarily driven by the existence of flow fluctuations. On the other hand we have shown that attracting vessel surfaces allow for the robust emergence of loops on their own. Even the full recovery of the initial plexus is feasible beyond the coupling induced nullity transition. This presents a new mechanism which allows for the maintenance of dissipation minimized reticulated vessel networks as long as there is an effective scaffold providing a positive growth feedback. No qualitative differences could be found in the phase diagrams in comparison with the dual diamond, or dual Laves graphs. The

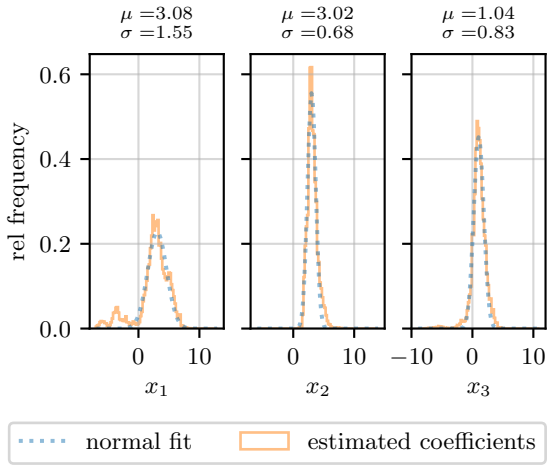

(a)

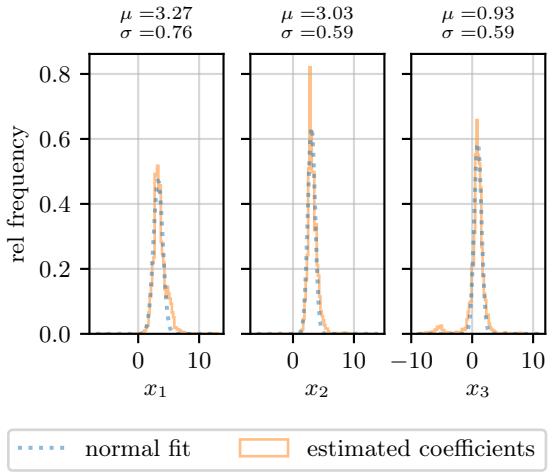

(b)

FIG. 10: Estimated parameters for the sinusoidal system near the central vein for $R = 397\mu m$, $\delta = 20\mu m$ and rescaled axis $x_i = log_{10}\lambda_i$ for the repulsive regime $\varepsilon = -1$ (a) and for the attractive regime $\varepsilon = 3$ (b) .

Lyapunov ansatz provides a generally applicable tool in network optimization, and should properly be tested for other boundary conditions or graph geometries which resemble realistic structures.

Our model may be interpreted as a toy-model for intertwined flow networks as found in the mammalian liver lobules and other organ structures, such as kidneys, pancreas or bone marrow. Our approach further enabled us to derive a more general form Murray's law, directly involving flow interactions and environmental interactions. We find this technique to predict the model parameters with high fidelity for simulated Kirchhoff networks given their topology and respective edge radii distributions. In the same manner we find reasonable order of magnitude estimates for the parameters in experimentally acquired data sets of sinusoids in liver lobule of mice. Hence one could use this methodology as an effective classification of spatially adapting network structures.

Eventually we strive towards a generalized formulation of environmental factors whose influence can be depicted in the form of local adaptation rules. We aim to expand the purely geometric approach which was studied here, by explicit involvement of hydrodynamic-chemical feedback between a vessel and its local environment. This would in particular concern entwined distribution networks transferring water and metabolites to their respective partner network. Biological systems such as the capillary networks in the liver lobule, present complex dual transport systems where the actual flow rates are not necessarily influenced by their respective partner network's flow rate [52] but rather by the concentration of bile salt components transported [26] as well as secretion rates of hepatocytes. Subsequently, future studies have to consider concentration/pump-rate dependent flow rate perturbations in the optimization model used so far. Also one should consider a direct postulation of cross-network feedback in the adaptation dynamics to account for the actual network structures. Recent studies regarding solute transport and optimization of cross-wall transport [27, 53] might present a suitable basis for that matter.

ACKNOWLEDGMENTS

Our thanks go to Hernan Morales-Navarrete (image reconstruction) and Fabian Segovia-Miranda (experiments) for providing us with the sinusoidal and canaliculial skeleton datasets. We'd like to thank Marino Zerial, Julien Delpierre, Quentin Vagne , Dora Tang, Andre Nadler, Mark Werner and all members of the Modes Lab and Zechner Lab for their comments, helpful discussions and resourceful feedback during the process of creating this work and draft.

[1] F. le Noble, V. Fleury, A. Pries, P. Corvol, A. Eichmann, and R. Reneman, Control of arterial branching morphogenesis in embryogenesis: go with the flow, Cardiovascular Research **65**, 619 (2005).

[2] D. Hu, D. Cai, A. V. Rangan, and C. M. Aegerter, Blood vessel adaptation with fluctuations in capillary flow distribution, PLoS ONE **7**, 1 (2012).

[3] H. Ronellenfitsch and E. Katifori, Phenotypes of vascular flow networks, Phys. Rev. Lett. **123**, 248101 (2019).

[4] W. Risau, Mechanisms of angiogenesis, Nature **386**, 671 (1997).

[5] P. Dimitrov and S. W. Zucker, A constant production hypothesis guides leaf venation patterning, Proceedings of the National Academy of Sciences **103**, 9363 (2006).

[6] T.-H. Nguyen, A. Eichmann, F. Le Noble, and V. Fleury, Dynamics of vascular branching morphogenesis: The effect of blood and tissue flow, Phys. Rev. E **73**, 061907 (2006).

[7] A. Lenard, S. Daetwyler, C. Betz, E. Ellertsdottir, H.-G. Belting, J. Huisken, and M. Affolter, Endothelial cell self-fusion during vascular pruning, PLOS Biology **13**, 1 (2015).

[8] A. Roth-Nebelsick, D. Uhl, V. Mosbrugger, and H. Kerp, Evolution and function of leaf venation architecture: A review, Annals of Botany **87**, 553 (2001).

[9] A. Tero, R. Kobayashi, and T. Nakagaki, A mathematical model for adaptive transport network in path finding by true slime mold, Journal of Theoretical Biology **244**, 553 (2007).

[10] C. D. Murray, The physiological principle of minimum work i. the vascular system and the cost of blood volume, Proceedings of the National Academy of Sciences **12**, 207 (1926).

[11] C. D. Murray, The physiological principle of minimum work ii. oxygen exchange in capillaries, Proceedings of the National Academy of Sciences **12**, 299 (1926).

[12] S. Bohn and M. O. Magnasco, Structure, scaling, and phase transition in the optimal transport network, Phys. Rev. Lett. **98**, 088702 (2007).

[13] E. Katifori, G. J. Szöllősi, and M. O. Magnasco, Damage and fluctuations induce loops in optimal transport networks, Phys. Rev. Lett. **104**, 048704 (2010).

[14] F. Corson, Fluctuations and redundancy in optimal transport networks, Phys. Rev. Lett. **104**, 048703 (2010).

[15] A. R. Pries, T. W. Secomb, and P. Gaehtgens, Structural adaptation and stability of microvascular networks: theory and simulations, American Journal of Physiology-Heart and Circulatory Physiology **275**, H349 (1998), pMID: 29591553.

[16] A. R. Pries, B. Reglin, and T. W. Secomb, Structural adaptation of vascular networks, Hypertension **38**, 1476 (2001).

[17] T. W. Secomb, J. P. Alberding, R. Hsu, M. W. Dewhirst, and A. R. Pries, Angiogenesis: An adaptive dynamic biological patterning problem, PLOS Computational Biology **9**, 1 (2013).

[18] D. Hu and D. Cai, Adaptation and optimization of biological transport networks, Phys. Rev. Lett. **111**, 138701 (2013).

[19] J. Gräwer, C. D. Modes, M. O. Magnasco, and E. Katifori, Structural self-assembly and avalanchelike dynamics in locally adaptive networks, Phys. Rev. E **92**, 012801 (2015).

[20] H. Ronellenfitsch and E. Katifori, Global optimization, local adaptation, and the role of growth in distribution networks, Phys. Rev. Lett. **117**, 138301 (2016).

[21] J. Haskovec, P. Markowich, and B. Perthame, Mathematical analysis of a pde system for biological network formation, Communications in Partial Differential Equations **40**, 918 (2015).

[22] J. Haskovec, P. Markowich, B. Perthame, and M. Schlottbom, Notes on a pde system for biological network formation, Nonlinear Analysis **138**, 127 (2016).

[23] G. B. West, J. H. Brown, and B. J. Enquist, A general model for the origin of allometric scaling laws in biology, Science **276**, 122 (1997).

[24] T. F. Sherman, On connecting large vessels to small. The meaning of Murray's law., Journal of General Physiology **78**, 431 (1981).

[25] W. W. Lautt, Regulatory processes interacting to maintain hepatic blood flow constancy: Vascular compliance, hepatic arterial buffer response, hepatorenal reflex, liver regeneration, escape from vasoconstriction, Hepatology Research **37**, 891 (2007).

[26] J. L. Boyer, Bile formation and secretion, in *Comprehensive Physiology* (American Cancer Society, 2013) pp. 1035–1078.

[27] K. Meyer, O. Ostrenko, G. Bourantas, H. Morales-Navarrete, N. Porat-Shliom, F. Segovia-Miranda, H. Nonaka, A. Ghaemi, J.-M. Verbavatz, L. Brusch, I. Sbalzarini, Y. Kalaidzidis, R. Weigert, and M. Zerial, A predictive 3d multi-scale model of biliary fluid dynamics in the liver lobule, Cell Systems **4**, 277 (2017).

[28] H. Morales-Navarrete, F. Segovia-Miranda, P. Klukowski, K. Meyer, H. Nonaka, G. Marsico, M. Chernykh, A. Kalaidzidis, M. Zerial, and Y. Kalaidzidis, A versatile pipeline for the multi-scale digital reconstruction and quantitative analysis of 3d tissue architecture, Elife **4**, e11214 (2015).

[29] M. M. Shah, R. V. Sampogna, H. Sakurai, K. T. Bush, and S. K. Nigam, Branching morphogenesis and kidney disease, Development **131**, 1449 (2004).

[30] F. C. Serluca, I. A. Drummond, and M. C. Fishman, Endothelial signaling in kidney morphogenesis: A role for hemodynamic forces, Current Biology **12**, 492 (2002).

[31] J. Magenheim, O. Ilovich, A. Lazarus, A. Klochendler, O. Ziv, R. Werman, A. Hija, O. Cleaver, E. Mishani, E. Keshet, and Y. Dor, Blood vessels restrain pancreas branching, differentiation and growth, Development **138**, 4743 (2011).

[32] A. Villasenor and O. Cleaver, Crosstalk between the developing pancreas and its blood vessels: An evolving dialog, Seminars in Cell & Developmental Biology **23**, 685 (2012), nutrient Sensing Pancreas Development.

[33] D. B. Azizoglu, D. C. Chong, A. Villasenor, J. Magenheim, D. M. Barry, S. Lee, L. Marty-Santos, S. Fu, Y. Dor, and O. Cleaver, Vascular development in the vertebrate pancreas, Developmental Biology **420**, 67 (2016).

[34] L. Planas-Paz and E. Lammert, Mechanosensing in Developing Lymphatic Vessels, in *Developmental Aspects of the Lymphatic Vascular System* (Springer Vienna, Vienna, 2013) pp. 23–40.

[35] K. K. Sivaraj and R. H. Adams, Blood vessel formation and function in bone, Development **143**, 2706 (2016).

[36] C. D. Modes, M. O. Magnasco, and E. Katifori, Extracting hidden hierarchies in 3d distribution networks, Phys. Rev. X **6**, 031009 (2016).

[37] L. Papadopoulos, P. Blinder, H. Ronellenfitsch, F. Klimm, E. Katifori, D. Kleinfeld, and D. S. Bassett, Comparing two classes of biological distribution systems using network analysis, PLOS Computational Biology **14**, 1 (2018).

[38] D. Akita, I. Kunita, M. D. Fricker, S. Kuroda, K. Sato, and T. Nakagaki, Experimental models for murray's law,

Journal of Physics D: Applied Physics **50**, 024001 (2016).
[39] L. D. Landau and E. M. Lifshits, Fluid Mechanics, by L.D. Landau and E.M. Lifshitz (1959).
[40] F. P. Kelly, D. R. Cox, and D. M. Titterington, Network routing, Philosophical Transactions of the Royal Society of London. Series A: Physical and Engineering Sciences **337**, 343 (1991).
[41] L. J. Grady and J. R. Polimeni, *Discrete Calculus*, Applied Analysis on Graphs for Computational Science (Springer Science & Business Media, 2010).
[42] R. Penrose, A generalized inverse for matrices (Cambridge University Press, 1955) p. 406–413.
[43] A. Ben-Israel and A. Charnes, Generalized inverses and the bott-duffin network analysis, Journal of Mathematical Analysis and Applications **7**, 428 (1963).
[44] R. Penrose, On best approximate solutions of linear matrix equations (Cambridge University Press, 1956) p. 17–19.
[45] C. A. Desoer and E. S. Kuh, *Basic circuit theory* (McGraw-Hill, New York [u.a.], 1969).
[46] W. T. Góźdź and R. Hołyst, Triply periodic surfaces and multiply continuous structures from the landau model of microemulsions, Phys. Rev. E **54**, 5012 (1996).
[47] V. Reitmann, *Mathematik für Ingenieure und Naturwissenschaftler* (Teubner, Stuttgart , Leipzig, 1996).
[48] H. Whitney, Non-Separable and Planar Graphs, Transactions of the American Mathematical Society **34**, 339 (1932).
[49] E. Jones, T. Oliphant, P. Peterson, *et al.*, SciPy: Open source scientific tools for Python (2001–), [Online; accessed 25. Februar 2020].
[50] H. Morales-Navarrete, H. Nonaka, A. Scholich, F. Segovia-Miranda, W. de Back, K. Meyer, R. L. Bogorad, V. Koteliansky, L. Brusch, Y. Kalaidzidis, F. Jülicher, B. M. Friedrich, and M. Zerial, Liquid-crystal organization of liver tissue, Elife **8**, 1035 (2019).
[51] H. Morales-Navarrete, H. Nonaka, F. Segovia-Miranda, M. Zerial, and Y. Kalaidzidis, Automatic recognition and characterization of different non-parenchymal cells in liver tissue, 2016 IEEE 13th International Symposium on Biomedical Imaging (ISBI) , 536 (2016).
[52] R. W. Brauer, G. F. Leong, and R. J. Holloway, Mechanics of Bile Secretion - Effect of Perfusion Pressure and Temperature on Bile Flow and Bile Secretion Pressure, American Journal of Physiology **177**, 103 (1954).
[53] F. J. Meigel and K. Alim, Flow rate of transport network controls uniform metabolite supply to tissue, Journal of The Royal Society Interface **15**, 20180075 (2018).
[54] G. H. Golub and V. Pereyra, The differentiation of pseudo-inverses and nonlinear least squares problems whose variables separate, SIAM Journal on Numerical Analysis **10**, 413 (1973).
[55] R. J. Duffin, Distributed and lumped networks, Journal of Mathematics and Mechanics **8**, 793 (1959).

Appendix A: Minimization of custom Lyapunov function Γ

To minimize the Lyapunov function Γ as given in section II we write it as

$$\Gamma = P + P' + E \tag{A1}$$

$$\text{with } P = \sum_e l \left[\frac{8\eta}{\pi} \frac{f_e^2}{r_e^4} + a r_e^2 \right] \tag{A2}$$

$$\text{and } P' = \sum_{e'} l' \left[\frac{8\eta'}{\pi} \frac{f_{e'}^2}{r_{e'}^4} + a' r_{e'}^2 \right] \tag{A3}$$

We may further use the vectorial notation for dissipation-volume terms P,P', using Ohms law to formulate it in terms of the nodal sinks/sources (here just for P, derivation for P' is performed analogously),

$$P = l \left[\boldsymbol{f}^T \boldsymbol{K}^{-1} \boldsymbol{f} + q\, Tr\left(\boldsymbol{K}^{1/2}\right) \right] \tag{A4}$$

$$= l \left[\boldsymbol{s}^T \left[\boldsymbol{B}^T \boldsymbol{K} \boldsymbol{B} \right]^\dagger \boldsymbol{s} + q\, Tr\left(\boldsymbol{K}^{1/2}\right) \right] \tag{A5}$$

with $q = a\left(\frac{8\eta}{\pi}\right)^{1/2}$ and $k_e = \frac{\pi r_e^4}{8\eta}$ as entries of the diagonal $\boldsymbol{K}$. We used $\boldsymbol{\Delta\varphi} = \boldsymbol{K}^{-1/2} \left[\boldsymbol{B} \cdot \boldsymbol{K}^{1/2}\right]^\dagger \boldsymbol{s}$ and $\boldsymbol{f} = \boldsymbol{K} \cdot \Delta\boldsymbol{\varphi}$. We calculate the (pseudo-)time derivatives of P to be

$$\frac{1}{l}\frac{dP}{dt} = \boldsymbol{s}^T \partial_t \left[\boldsymbol{B} \cdot \boldsymbol{K} \cdot \boldsymbol{B}^T\right]^\dagger \boldsymbol{s} + 2\boldsymbol{s}^T \left[\boldsymbol{B} \cdot \boldsymbol{K} \cdot \boldsymbol{B}^T\right]^\dagger \partial_t \boldsymbol{s} + q \partial_t Tr\left(\boldsymbol{K}^{1/2}\right) \tag{A6}$$

The derivative of the generalized inverse $\boldsymbol{B} \cdot \boldsymbol{K} \cdot \boldsymbol{B}^T = \boldsymbol{A}$ being [54],

$$\begin{aligned} \partial_t \boldsymbol{A}^\dagger = &-\boldsymbol{A}^\dagger \left(\boldsymbol{B} \cdot \partial_t \boldsymbol{K} \cdot \boldsymbol{B}^T\right) \boldsymbol{A}^\dagger \\ &+ \left[\boldsymbol{I} - \boldsymbol{A}^\dagger \cdot \boldsymbol{A}\right] \left(\boldsymbol{B} \cdot \partial_t \boldsymbol{K} \cdot \boldsymbol{B}^T\right) \boldsymbol{A}^{T\dagger} \cdot \boldsymbol{A}^\dagger \\ &+ \boldsymbol{A}^\dagger \cdot \boldsymbol{A}^{T\dagger} \left(\boldsymbol{B}^T \cdot \partial_t \boldsymbol{K} \cdot \boldsymbol{B}\right) \left[\boldsymbol{I} - \boldsymbol{A} \cdot \boldsymbol{A}^\dagger\right] \end{aligned} \tag{A7}$$

Fortunately the projector terms vanish as we have,

$$\boldsymbol{s}^T \left[\boldsymbol{I} - \boldsymbol{A}^\dagger \cdot \boldsymbol{A}\right] = 0 \text{ and } \left[\boldsymbol{I} - \boldsymbol{A} \cdot \boldsymbol{A}^\dagger\right] \boldsymbol{s} = 0 \tag{A8}$$

Together with the identity $\boldsymbol{A}^\dagger = \left(\boldsymbol{A}^T\right)^\dagger$ the total time-derivative of P becomes,

$$\frac{1}{l}\frac{dP}{dt} = -\boldsymbol{s}^T \boldsymbol{A}^{T\dagger} \left(\boldsymbol{B} \cdot \partial_t \boldsymbol{K} \cdot \boldsymbol{B}^T\right) \boldsymbol{A}^\dagger \boldsymbol{s} + 2\boldsymbol{s}^T \boldsymbol{A}^\dagger \partial_t \boldsymbol{s} + q \partial_t Tr\left(\boldsymbol{K}^{1/2}\right) \tag{A9}$$

With partial derivatives simplifying this formula as:

$$\partial_t Tr\left(\boldsymbol{K}^{1/2}\right) = \frac{1}{2} Tr\left(\boldsymbol{K}^{-1/2} \cdot \partial_t \boldsymbol{K}\right) \tag{A10}$$

$$\partial_t \boldsymbol{s} = 0 \tag{A11}$$

As $\Delta\boldsymbol{\varphi} = \boldsymbol{B}^T \cdot \boldsymbol{A}^\dagger \boldsymbol{s}$, we may write the total time-derivative as

$$\frac{1}{l}\frac{dP}{dt} = -\Delta\boldsymbol{\varphi}^T \cdot \partial_t \boldsymbol{K} \cdot \Delta\boldsymbol{\varphi} + \frac{q}{2} Tr\left(\boldsymbol{K}^{-1/2}\partial_t \boldsymbol{K}\right) \quad \text{(A12)}$$

With $\partial_t K_{ee} = \frac{\pi r_e^3}{2\eta}\partial_h r_e$ and re-substituting q this becomes

$$\frac{1}{l}\frac{dP}{dt} = \frac{\pi}{2\eta}\sum_e r_e\left[\frac{4a\eta}{\pi} - \Delta\varphi_e^2 r_e^2\right]\partial_t r_e \quad \text{(A13)}$$

The coupling component's derivative E may be calculated with partial derivatives,

$$\frac{E}{dt} = -\frac{b\varepsilon}{2}\left[\sum_{ee'} F_{ee'}\Delta r_{ee'}^{\varepsilon-1}\partial_t r_e + \sum_{ee'} F_{ee'}\Delta r_{ee'}^{\varepsilon-1}\partial_t r_{e'}\right] \quad \text{(A14)}$$

so combining (A13) and (A14) we get for the total derivative of Γ,

$$\begin{aligned}\frac{d\Gamma}{dt} &= \frac{\pi l}{2\eta}\sum_e r_e\left[\frac{4a\eta}{\pi} - \Delta\varphi_e^2 r_e^2\right] r_e\partial_t r_e \\ &+ \frac{\pi l'}{2\eta'}\sum_{e'}\left[\frac{4a'\eta'}{\pi} - \Delta\varphi_{e'}^2 r_{e'}^2\right] r_{e'}\partial_t r_{e'} \\ &- \frac{b\varepsilon}{2}\left[\sum_e F_{ee'}\Delta r_{ee'}^{\varepsilon-1}\partial_t r_e + \sum_{e'} F_{ee'}\Delta r_{ee'}^{\varepsilon-1}\partial_t r_{e'}\right]\end{aligned} \quad \text{(A15)}$$

We then acquire the ODE system presented in the main body of our paper by setting $\alpha = \frac{4a\eta}{\pi}$ and $\beta = \frac{b\eta|\varepsilon|}{\pi l}$ and α', β' accordingly,

$$\begin{aligned}\frac{d\Gamma}{dt} &= \frac{\pi l}{2\eta}\sum_e\Bigg(\left[\alpha - \Delta\varphi_e^2 r_e^2\right] r_e \\ &-\beta sgn\left(\varepsilon\right)\sum_{e'} F_{ee'}\Delta r_{e'}^{\varepsilon-1}\Bigg)\partial_t r_e \\ &+\frac{\pi l'}{2\eta'}\sum_{e'}\Bigg(\left[\alpha' - \Delta\varphi_{e'}^2 r_{e'}^2\right] r_{e'} \\ &-\beta' sgn\left(\varepsilon\right)\sum_e F_{ee'}\Delta r_{ee'}^{\varepsilon-1}\Bigg)\partial_t r_{e'}\end{aligned} \quad \text{(A16)}$$

To find a local minimum of Γ when progressing through (pseudo-)time h we we have to ensure that $d\Gamma \leq 0$. So we may minimize the Lyapunov function, with auxiliary functions χ, $\chi' \geq 0$ by choosing

$$\partial_t r_e = \chi\left(\left[\Delta\varphi_e^2 r_e^2 - \alpha\right] r_e + \beta sgn\left(\varepsilon\right)\sum_{e'} F_{ee'}\Delta r_{ee'}^{\varepsilon-1}\right) \quad \text{(A17)}$$

$$\partial_t r_{e'} = \chi'\left(\left[\Delta\varphi_{e'}^2 r_{e'}^2 - \alpha'\right] r_{e'} + \beta' sgn\left(\varepsilon\right)\sum_e F_{ee'}\Delta r_{ee'}^{\varepsilon-1}\right) \quad \text{(A18)}$$

Appendix B: Uncorrelated and coupled flow fluctuations

In this section we give a detailed derivation of the analytic form of the mean squared pressure in case of uncorrelated, identically distributed sink fluctuations as introduced in [14] and discussed in section II.
From the current law (1) in combination with Ohm's law (2) one knows that the sum over all in and outflows of the system vanishes[55], i.e. $\sum_j s_j = 0$. When considering the sink conditions as well as the source constraint defined in the theory section, we may write the moments as (putting the distinguished source at $j = 0$),

$$\langle s_j\rangle = \mu \quad \text{(B1)}$$

$$\langle s_0\rangle = -\left\langle\sum_{j>0} s_j\right\rangle = (1-n)\,\mu \quad \text{(B2)}$$

$$\langle s_j s_k\rangle = \delta_{jk}\sigma^2 + \mu^2 \text{ if } j,k > 0 \quad \text{(B3)}$$

$$\langle s_0^2\rangle = \left\langle\sum_{j,k>0} s_j s_k\right\rangle = (n-1)\,\sigma^2 + (n-1)^2\,\mu^2 \quad \text{(B4)}$$

$$\langle s_0 s_k\rangle = -\left\langle\sum_{j>0} s_j s_k\right\rangle = -(n-1)\,\mu^2 - \sigma^2 \quad \text{(B5)}$$

Hence we may calculate the squared-mean pressure by using the auxiliary conductivity tensor $\boldsymbol{A}_{jk}^e = \boldsymbol{K}_{ee}^{-1}\left[\boldsymbol{B}\cdot\boldsymbol{K}^{1/2}\right]_{ej}^\dagger\left[\boldsymbol{B}\cdot\boldsymbol{K}^{1/2}\right]_{ek}^\dagger$ as,

$$\langle\Delta\varphi_e^2\rangle = \sum_{jk}\boldsymbol{A}_{jk}^e\langle s_j s_k\rangle \quad \text{(B6)}$$

$$= \boldsymbol{A}_{00}^e\langle s_0^2\rangle + 2\sum_{j>0}\boldsymbol{A}_{j0}^i\langle s_0 s_j\rangle + \sum_{j,k>0}\boldsymbol{A}_{jk}^i\langle s_j s_k\rangle \quad \text{(B7)}$$

$$\begin{aligned}&= \boldsymbol{A}_{00}^e(n-1)\left[(n-1)\,\mu^2 + \sigma^2\right] \\ &\quad - 2\sum_{j>0}\boldsymbol{A}_{j0}^e\left[(n-1)\,\mu^2 + \sigma^2\right] \\ &\quad + \sum_{j,k>0}\boldsymbol{A}_{jk}^e\left[\delta_{jk}\sigma^2 + \mu^2\right]\end{aligned} \quad \text{(B8)}$$

$$\begin{aligned}&= \sum_{j,k}\boldsymbol{A}_{jk}^e(n-1)\left[(n-1)\,\mu^2 + \sigma^2\right]\delta_{0j}\delta_{0k} \\ &\quad - \sum_{j,k}\boldsymbol{A}_{jk}^e\left[(n-1)\,\mu^2 + \sigma^2\right]\left[(1-\delta_{0k})\,\delta_{0j} + (1-\delta_{0j})\,\delta_{0k}\right] \\ &\quad + \sum_{j,k}\boldsymbol{A}_{jk}^e\left[\delta_{jk}\sigma^2 + \mu^2\right](1-\delta_{0j})\,(1-\delta_{0k})\end{aligned} \quad \text{(B9)}$$

Ordering the terms for μ and σ respectively we can acquire the coefficient matrices $\boldsymbol{U}$ and $\boldsymbol{V}$,

$$\begin{aligned}\langle\Delta\varphi_e^2\rangle &= \sum_{j,k} \boldsymbol{A}^e_{jk}\mu^2 \Big[(1-\delta_{0j})(1-\delta_{0k}) + \delta_{0j}\delta_{0k}(n-1)^2 \\ &\quad - (n-1)\left(\delta_{0j}(1-\delta_{0k}) + \delta_{0k}(1-\delta_{0j})\right)\Big] \\ &\quad + \sum_{j,k} \boldsymbol{A}^e_{jk}\sigma^2 \left[(1-\delta_{0k})(1-\delta_{0j})\delta_{jk} - \delta_{0j}(1-\delta_{0k})\right. \\ &\quad \left. -\delta_{0k}(1-\delta_{0j}) + (n-1)\delta_{0j}\delta_{0k}\right] \qquad \text{(B10)} \\ &= \sum_{j,k} \boldsymbol{A}^e_{jk}\mu^2 \left[1 + \delta_{0j}\delta_{0k}n^2 - n(\delta_{0j}+\delta_{0k})\right] \\ &\quad + \sum_{j,k} \boldsymbol{A}^e_{jk}\sigma^2 \left[\delta_{jk} + (n+1+\delta_{jk})\delta_{0j}\delta_{0k}\right. \\ &\quad \left. - (1+\delta_{jk})(\delta_{0j}+\delta_{0k})\right] \qquad \text{(B11)}\end{aligned}$$

We further suggest to expand this ansatz by introducing additional sources which act as clones of the very first one, i.e. we will have $s_p = s_q$ using the indices p, q for sources and u, v for sinks. Then conditions (B2), (B4),(B5) will become for a sources and b sinks (with $a + b = n$),

$$\left\langle \sum_p s_p \right\rangle = -\left\langle \sum_u s_u \right\rangle = -b\mu \rightarrow \langle s_p \rangle = -\frac{b}{a}\mu \qquad \text{(B12)}$$

$$\langle s_p s_q \rangle = \frac{1}{a^2}\left\langle \sum_{u,v} s_u s_v \right\rangle = \frac{1}{a^2}\left(b\sigma^2 + b^2\mu^2\right) \qquad \text{(B13)}$$

$$\langle s_p s_u \rangle = -\frac{1}{a}\left\langle \sum_v s_v s_u \right\rangle = -\frac{1}{a}\left(b\mu^2 - \sigma^2\right) \qquad \text{(B14)}$$

And hence we may calculate the mean squared pressure and its coefficient matrices respectively as,

$$\begin{aligned}\langle\Delta\varphi_e^2\rangle &= \sum_{j,k} \boldsymbol{A}^e_{jk}\mu^2 \left[\frac{b^2}{a^2}\sum_{pq}\delta_{pj}\delta_{qk}\right. \\ &\quad \left. -\frac{b}{a}\sum_{pu}(\delta_{pj}\delta_{uk} + \delta_{uj}\delta_{pk}) + \sum_{uv}\delta_{uj}\delta_{vk}\right] \\ &\quad + \sum_{j,k} \boldsymbol{A}^e_{jk}\sigma^2 \left[\frac{b}{a^2}\sum_{pq}\delta_{pj}\delta_{qk}\right. \\ &\quad \left. -\frac{1}{a}\sum_{pu}(\delta_{pj}\delta_{uk} + \delta_{uj}\delta_{pk}) + \sum_{uv}\delta_{uj}\delta_{vk}\delta_{uv}\right] \qquad \text{(B15)}\end{aligned}$$

Appendix C: Simulating coupled, adapting networks

In this section we show additional material of the simulations' results as performed in section III for both of the networks in comparison. In Figure 11 and 12 we display the nullity transition curves for the cases of repulsive and attractive coupling. It may be noted here once again that all simulation parameters λ_i were initialized identically for the two networks, meaning any deviations in ϱ have to be caused by topological differences. This phenomenon in particular apparent in the case of attractive coupling in cubic lattices where the nullity transition in the respective networks becomes smeared out differently for the two structures. Repeating the simulations for coupled networks consisting of complimentary Laves graphs or diamond lattices, we find this effect negligible. In Figure 13 we display the shift of the nullity onsets for the dominating interaction mechanisms. In the case of repulsive coupling 13a, both networks display a shift of the onset of fluctuation induced loops as well as a shift of the estimated saturation point. It may be noted though that a change of several orders of magnitude in the coupling λ_1 is necessary in order to shift the fluctuation onset at all. It is nevertheless crucial to note that the overall nullity is reduced even in the saturated case which itself tends to be achieved only for significantly higher fluctuations λ_3. A similar trend of shifting may be observed in the case of attractive coupling 13b. The onset of full plexus recovery as well as the saturation onset are developing on similar scales though. In particular interesting seems to be the trajectories for network # 2 as they suggest the

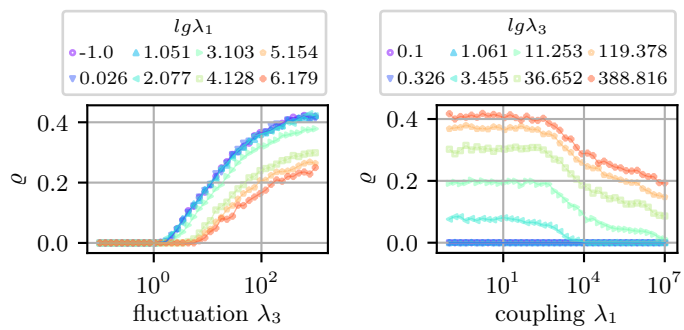

(a) Network # 1

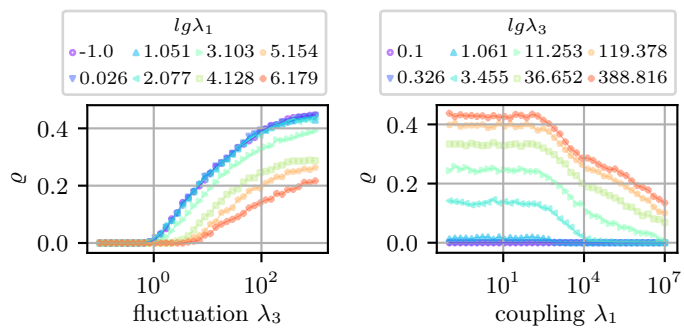

(b) Network # 2

FIG. 11: Nullity ϱ transitions for repulsively coupled networks ($\varepsilon = -1$): Symmetric fluctuation λ_3 induced nullity onset and coupling λ_1 induced nullity breakdown for the two networks (a) and (b)

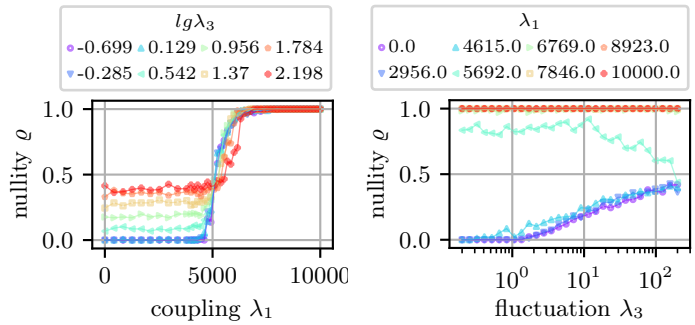

(a) Network # 1

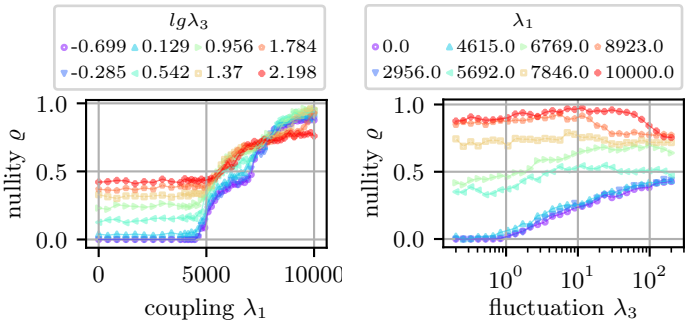

(b) Network # 2

FIG. 12: Nullity ϱ transitions for attractively coupled networks ($\varepsilon = 3$): Slightly asymmetric coupling λ_1 induced nullity onset and fluctuation λ_3 induced nullity transition for the two networks (a) and (b)

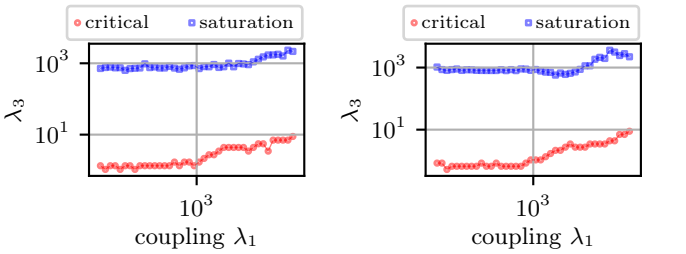

(a) Repulsive Coupling

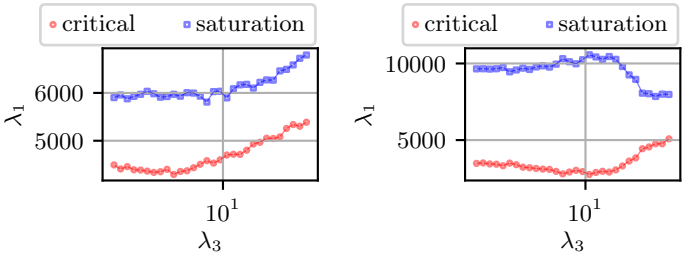

(b) Attractive Coupling

FIG. 13: Shift of onset and saturation points for coupled networks and their dominant interactions, network # 1 on the left and # 2 on the right: (a) Negative coupling exponent $\varepsilon = -1$, shift of fluctuation λ_3 induced nullity transition. (b) Positive coupling exponent $\varepsilon = 3$, shift of fluctuation λ_1 induced nullity transition.

possibility of a re-entry behaviour between coupling and fluctuation dominated nullity regimes.

Appendix D: Scaling laws in coupled, noisy networks

This section centers around the scaling law discussed in section IV. One can show that introducing fluctuations and coupling alter the classical form of Murray's Law $r_0^3 = r_1^3 + r_2^3$ in the following way: Given the Kirchhoff current law and rewriting it via Ohm's law, we get for all sink-vertices i,

$$\sum_e B_{ie} f_e = s_i \Leftrightarrow \sum_e B_{ie} r_e^{*4} \Delta\varphi_e^* = s_i^* \tag{D1}$$

Taking the average over all pressure configurations between two adaptation events we get

$$\sum_e B_{ie} r_e^{*4} \langle \Delta\varphi_e^* \rangle = \langle s_i^* \rangle \Leftrightarrow \sum_e \Theta_{ie} r_e^{*4} |\langle \Delta\varphi_e^* \rangle| = \langle s_i^* \rangle \tag{D2}$$

with an effective incidence factor $\Theta_{ie} = \begin{cases} \pm 1 \\ 0 \end{cases}$ distinguishing between in- and outgoing flows on the relevant edges, see Figure 14. In order to acquire the cubic form we substitute r_e^* with the result of the stationary state's equations,

$$\partial_{t^*} r_e^* = 0 \tag{D3}$$

$$\Rightarrow 0 = \left(r_e^{*2} \langle \Delta\varphi_e^{*2} \rangle - \lambda_2 \right) r_e^* + \lambda_1 sgn(\varepsilon) \sum_{ee'} F_{ee'} \Delta r_{ee'}^{*,-\varepsilon} \tag{D4}$$

$$\Leftrightarrow r_e^* = \frac{\sqrt{\lambda_2 - \lambda_1 r_e^{*-1} sgn(\varepsilon) \sum_{ee'} F_{ee'} \Delta r_{ee'}^{*,\varepsilon-1}}}{\sqrt{\langle \Delta\varphi_e^{*2} \rangle}} \tag{D5}$$

Plugging (D5) into (D2) and rewriting $|\langle \Delta\varphi_e^* \rangle| = \sqrt{\langle \Delta\varphi_e^* \rangle^2}$, $g_e^*(\varepsilon) = sgn(\varepsilon) \sum_{ee'} F_{ee'} \Delta r_{ee'}^{*,\varepsilon-1}$ we get,

$$\sum_e \Theta_{ie} \sqrt{\left(\lambda_2 - \lambda_1 r_e^{*-1} g_e^*(\varepsilon) \right) \frac{\langle \Delta\varphi_e^* \rangle^2}{\langle \Delta\varphi_e^{*2} \rangle}} r_e^{*3} = \langle s_i^* \rangle \tag{D6}$$

We know from section B that $\langle \Delta\varphi_e^2 \rangle = \sum_{jk} \boldsymbol{A}_{jk}^e \langle s_j s_k \rangle$ and may also deduce $\langle \Delta\varphi_e \rangle^2 = \sum_{jk} \boldsymbol{A}_{jk}^e \langle s_j \rangle \langle s_k \rangle$. This

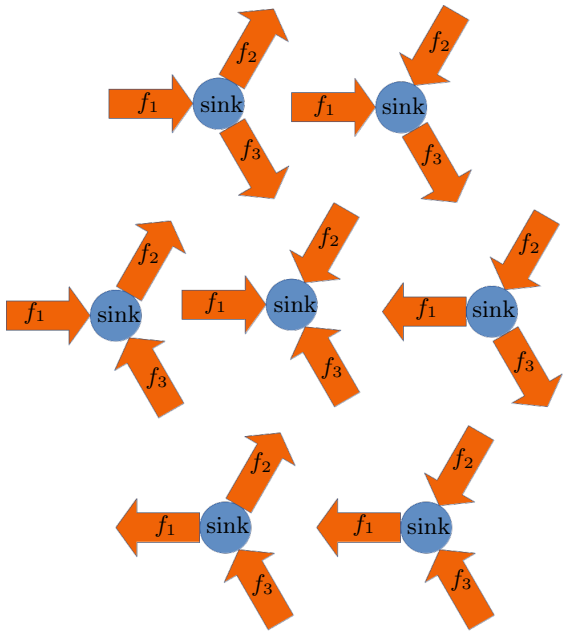

FIG. 14: Scheme of identifying different flow combinations at a sink determining the respective sign of Θ_{ie}, here shown for Y-branching point. Let's identify the sink as $i = 0$ and and the respective flow carrying edges as $e \in \{1, 2, 3\}$ and define an incidence triplet $\boldsymbol{\Theta} = (\Theta_{01}, \Theta_{02}, \Theta_{03})$. Reading from left to right we have in the top diagram:
$\boldsymbol{\Theta} = (1, -1, -1)$, $\boldsymbol{\Theta} = (1, 1, -1)$
Middle diagram:
$\boldsymbol{\Theta} = (1, -1, 1)$, $\boldsymbol{\Theta} = (1, 1, 1)$, $\boldsymbol{\Theta} = (-1, 1, -1)$
Bottom diagram:
$\boldsymbol{\Theta} = (-1, -1, 1)$, $\boldsymbol{\Theta} = (-1, 1, 1)$

enables us to calculate the ratio via the covariance,

$$\frac{\langle \Delta\varphi_e^2 \rangle}{\langle \Delta\varphi_e \rangle^2} = \frac{\sum_{jk} \boldsymbol{A}^e_{jk} \langle s_j s_k \rangle}{\sum_{jk} \boldsymbol{A}^e_{jk} \langle s_j \rangle \langle s_k \rangle} \tag{D7}$$

$$= \frac{\sum_{jk} \boldsymbol{A}^e_{jk} \left[\langle s_j \rangle \langle s_k \rangle + \langle (s_j - \langle s_j \rangle)(s_k - \langle s_k \rangle) \rangle \right]}{\sum_{jk} \boldsymbol{A}^e_{jk} \langle s_j \rangle \langle s_k \rangle} \tag{D8}$$

$$= 1 + \frac{\sum_{jk} \boldsymbol{A}^e_{jk} \langle (s_j - \langle s_j \rangle)(s_k - \langle s_k \rangle) \rangle}{\sum_{jk} \boldsymbol{A}^e_{jk} \langle s_j \rangle \langle s_k \rangle} \tag{D9}$$

Substituting this into (D6) and having $\frac{\langle \Delta\varphi_e^2 \rangle}{\langle \Delta\varphi_e \rangle^2} = \frac{\langle \Delta\varphi_e^{*2} \rangle}{\langle \Delta\varphi_e^* \rangle^2}$, $H_e = \frac{\sum_{jk} \boldsymbol{A}^e_{jk} \langle (s_j - \langle s_j \rangle)(s_k - \langle s_k \rangle) \rangle}{\sum_{jk} \boldsymbol{A}^e_{jk} \langle s_j \rangle \langle s_k \rangle}$ we get,

$$\sum_e a_e r_e^{*3} = \langle s_i^* \rangle \tag{D10}$$

$$\text{setting } a_e = \Theta_{ie} \sqrt{\frac{\lambda_2 - \lambda_1 r_e^{*-1} g_e^*(\varepsilon)}{1 + H_e}} \tag{D11}$$

One may simplify this complex by considering the following: Assume that we have all randomly fluctuating sinks distributed uncorrelated yet identically as in section B, (B11), then we may set $\langle s_i^* \rangle = 1$ and reevaluate H_e. This leads to the equation presented in section IV,

$$\sum_e a_e r_e^{*3} = 1 \tag{D12}$$

$$\text{with } a_e = \Theta_{ie} \sqrt{\frac{\lambda_2 - \lambda_1 r_e^{*-1} g_e^*(\varepsilon)}{1 + \lambda_3 \frac{\delta\phi_e}{\phi_e}}} \tag{D13}$$

For experimental validation of (D12) it will be necessary to know the networks vessel radii as well as the sink/source pattern (although it may be sufficient to know where the system's source is and to consider every other node as sink). Considering Y-branchings of low sink/source value (points of negligible secretion/leakage) such that $|a_e r_e^{*,3}| \gg 1$, further setting the index for the largest vessel to zero (and accordingly increasing for the other vessel pieces at the branching) may write,

$$a_0 r_0^{*3} = a_1 r_1^{*3} + a_2 r_2^{*3} \tag{D14}$$

In Figure 15 we show the applied reduction procedure as used in the section IV B. First, the vertices in the sinusoidal network (SI) which are closest to the central

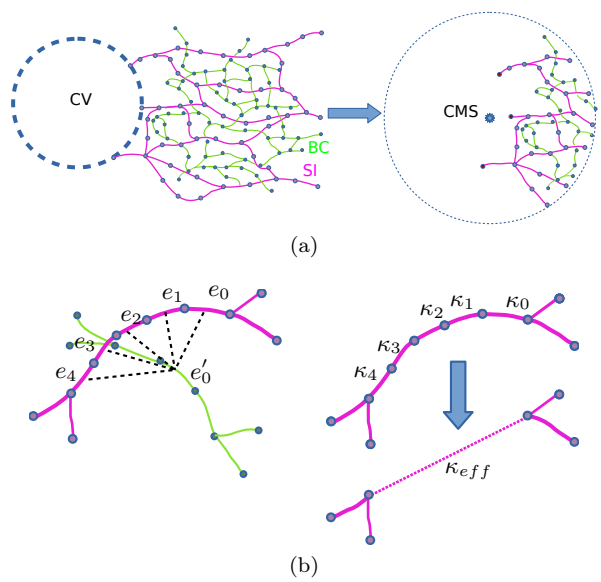

FIG. 15: Setting the range of interest and coarse-graining the sinusoidal (SI) and bile canaliculi system (BC): (a) Left: Vertices closest to the central vein (CV) are identified as sinks. Right: Determine geometric center of mass of all sinks (CMS) and discard all components, vertices, edges outside a set perimeter. (b) Left: Deducting the distance of one path of a network to another path of the partner network by calculating the pair-wise distances of all path-segments and finding its minimum. Right: Coarse-graining paths into one effective edge, with new edge weight according to addition theorem $\kappa_{eff} = \sum_i \frac{1}{\kappa_i}$.

vein (CV) are identified. Using these a geometric center of mass(CMS) is calculated and used as the center of a sphere of radius R, representing the range of interest (ROI). Any other components,vertices or edges of any network positioned ROI, see Figure 15a. Next, all branching points in the sinusoidal network are identified and all paths $\boldsymbol{p} = (e_i, ..., e_j)$ consisting of edges e_i which start from these points. We proceed for the canaliculi the same way and then check for each segment of a path $\boldsymbol{p}$ whether there is another segment of another network's path $\boldsymbol{p}'$ inside a perimeter δ . If so, these paths count as affiliated. Then we merge all edges along a path towards a single edge by using the conventional addition theorems for series of conductivities, as $\kappa_{eff} = \sum_i \frac{1}{\kappa_i}$, see Figure 15b. When confronted with datasets of real spatial transport network such as blood capillaries and secretion channels in IV B it becomes important to note that the chosen ROI, namely the radius R and the affiliation perimeter δ will affect the estimation of the parameters $x_i = log\,(\lambda_i)$. In Figure 16 and 17 we present the results for the fitted parameters' means μ and standard deviations σ for the cases of repulsive and attractive interactions for various R, δ (numerically acquired gaussian fits as shown in the main section IV B). As can be seen increasing the affiliation parameter δ will naturally increase the number of edges affiliated with each other, possibly linking vessel structures of several consecutive neighbourhoods, see Figure 18. This seems to cause considerable increase of the means of the effective volume penalty x_2 yet no major change for the estimated effective fluctuation x_3 for any coupling type. Nevertheless, depending on the type of coupling we see little (repulsive) to major increases (attractive) in the effective coupling x_1. The size of the range of interest R doesn't really affect the overall found parameters x_2 and x_3 yet fluctuations in the estimation of x_1 become visible.

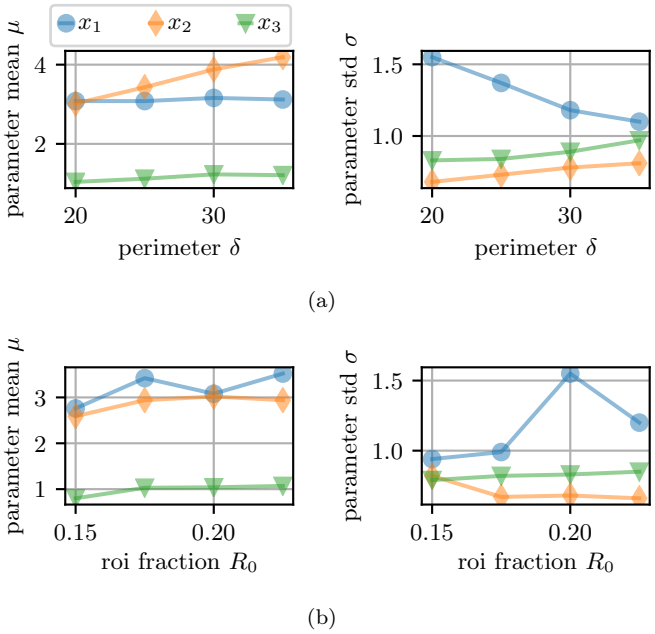

FIG. 16: Estimated parameters $x_i = log_{10}\lambda_i$ in sinusoids considering repulsive coupling $\varepsilon = -1$. (a) : Perimeter δ dependency of the estimated adaptation parameters for set range of interest $R = 0.2R_0 = 397\mu m$, where R_0 is the network's maximum extent including the entire dataset. (b) : Range of interest R dependency of the estimated adaptation parameters for a set perimeter $\delta = 20\mu m$.

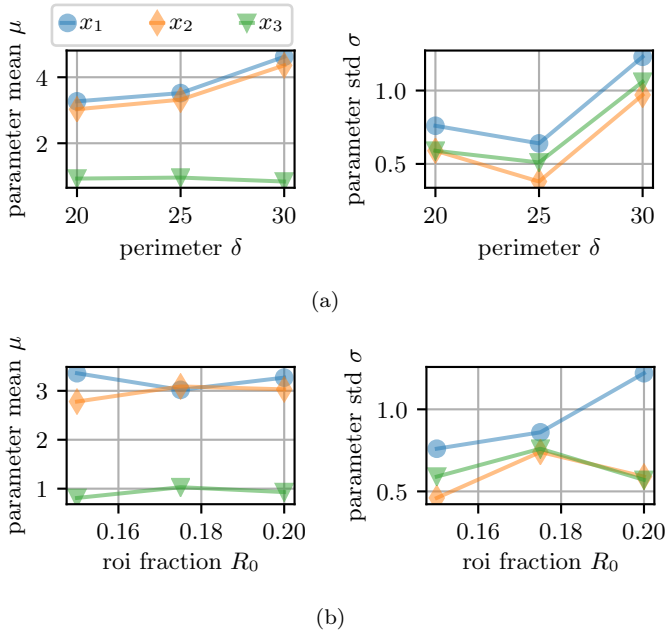

FIG. 17: Estimated parameters $x_i = log_{10}\lambda_i$ in sinusoids considering attractive coupling $\varepsilon = 3$. (a) : Perimeter δ dependency of the estimated adaptation parameters for set range of interest $R = 0.2R_0 = 397\mu m$, where R_0 is the network's maximum extent including the entire dataset. (b) : Range of interest R dependency of the estimated adaptation parameters for a set perimeter $\delta = 20\mu m$.

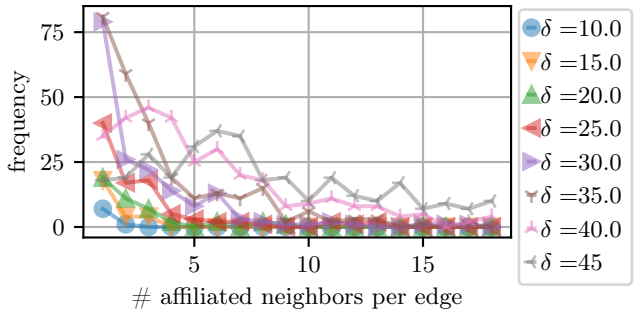

FIG. 18: Histogram displaying the number of affiliated neighbors (edges) found for a given radius around a vessel (threshold, all values the inset in μm). Total number of pairings found overall for given threshold in the inset for set range of interest $R = 0.2R_0$.